

1 **The local amplification of surface waves: A new observable to constrain elastic**
2 **velocities, density, and anelastic attenuation**

3 Fan-Chi Lin¹, Victor C. Tsai¹, and Michael H. Ritzwoller²

4 ¹Seismological Laboratory, Division of Geological and Planetary Sciences, California
5 Institute of Technology, Pasadena, CA 91125, USA. (linf@caltech.edu)

6 ²Center for Imaging the Earth's Interior, Department of Physics, University of Colorado
7 at Boulder, Boulder, CO 80309-0390, USA

8 **Abstract**

9 The deployment of USArray across the continental US has prompted developments
10 within surface wave tomography to exploit this unprecedented dataset. In this study, we
11 present a method to measure a new surface-wave observable: broadband surface-wave
12 amplification maps which is distinct from traditional phase and group velocity
13 measurements and potentially may provide new and unique constraints on elastic
14 velocities and density within the crust and upper mantle. The method, similar to its phase
15 velocity counterpart referred to as Helmholtz tomography, initiates by constructing phase
16 travel time and amplitude maps across the array for each period and earthquake. Spatial
17 differential operators are then applied to evaluate the amplitude variation, as well as the
18 effect of focusing/defocusing. Based on the 2D damped wave equation, the amplitude
19 variation corrected for focusing/defocusing is directly linked to both local amplification
20 and intrinsic attenuation, but the two may be separated by examining waves propagating
21 in different directions. We apply the method to teleseismic Rayleigh waves observed
22 across USArray between 24 and 100-sec period. We show that the observed amplification

1 maps are strongly correlated with known geological features and although small-scale
2 attenuation measurements may be contaminated by complex wave phenomena, larger
3 scale anelastic attenuation can be estimated reliably. In addition, the observed
4 amplification maps compare well with predictions based on recent 3D shear velocity
5 models. The predictions based on two models with different prescribed density structure
6 are compared, demonstrating the potential for using estimates of local amplification to
7 constrain not only 3D velocity structure but also density.

8 **1. Introduction**

9 Surface waves, which propagate near the earth's surface, are sensitive to the elastic,
10 anelastic, and density structure of the crust and upper mantle. Most surface-wave
11 tomography studies investigate shear velocity structure by measuring the group and phase
12 travel times of surface-waves (e.g. [Trampert & Woodhouse 1996](#); [Ekstrom et al. 1997](#);
13 [Shapiro et al. 2005](#); [Lin et al. 2011a](#)). Due to the complexity of source, path, and receiver
14 effects, studies based on amplitude measurements to infer velocity structure (e.g. [Dalton](#)
15 [& Ekstrom 2006a](#); [Yang & Forsyth 2006a](#); [Pollitz & Snoke 2010](#); [Lin & Ritzwoller](#)
16 [2011a](#)) and anelastic structure (e.g. [Dalton & Ekstrom 2006b](#); [Yang & Forsyth 2008](#);
17 [Lawrence & Prieto 2011](#); [Lin et al. 2011b](#)) are relatively less common. One of the
18 reasons that such studies are less common is that seismometers are usually more poorly
19 calibrated in amplitude than in phase. Although surface waves are sensitive to density
20 structure within the crust and uppermost mantle, the estimation of density is typically
21 considered to be too difficult using surface waves information alone ([Tanimoto 1991](#)).
22 Instead, some authors have approached the problem by jointly interpreting surface wave
23 dispersion measurements along with gravity (e.g. [Maceira & Ammon 2009](#)). Estimation

1 of the distribution of density and anelastic attenuation in 3D is highly desirable, however,
2 because this information would place new constraints on in situ temperature and
3 composition and, perhaps even more intriguingly, would present a means to evaluate
4 fundamental geodynamic driving forces.

5 The recent deployment of the USArray Transportable Array ([Fig. 1a](#)) across the US
6 permits the study of the broadband surface-wave wavefield in greater detail than ever
7 possible before on continental scales (e.g. [Pollitz 2008](#), [Liang & Langston 2009](#)). By
8 taking advantage of the 2D array configuration and the approximately 2D nature of
9 surface wave propagation ([Tanimoto 1990](#); [Wielandt 1993](#); [Tromp & Dahlen 1993](#)), we
10 have developed two new tomographic methods referred to as eikonal and Helmholtz
11 tomography ([Lin et al. 2009](#); [Lin & Ritzwoller 2011a](#)). The methods estimate
12 directionally-dependent phase velocity by locally applying the 2D wave equation based
13 on phase travel time and amplitude measurements. The methods start by empirically
14 constructing phase travel time and amplitude maps for surface waves emitted by an
15 earthquake or observed on inter-station cross-correlations for ambient noise ([Lin et al.](#)
16 [2009](#)). Spatial differential operators (the gradient and Laplacian) are then applied to the
17 travel time and amplitude fields to estimate the apparent velocity and corrections for
18 finite frequency effects. This type of local inversion method mitigates the need to model
19 the source mechanism and structure outside of the array by focusing explicitly on local
20 wave propagation ([Pollitz & Snoke 2010](#)). The methods have been applied successfully
21 to USArray data to resolve high-resolution 3D isotropic and anisotropic structures in the
22 crust and upper mantle across the western US ([Moschetti et al. 2010a](#); [Moschetti et al.](#)
23 [2010b](#); [Lin et al. 2011a](#)).

1 In the present study, we extend these tomographic methods to study the local
2 amplification and anelastic attenuation of surface waves, which potentially provides
3 independent new constraints on the elastic velocities, density, and anelastic structure of
4 the crust and upper mantle compared to traditional phase and group velocity tomography.
5 The local amplification, sometimes also referred to as the receiver term or local site
6 response (e.g. Dalton & Ekstrom 2006b; Yang & Forsyth 2006a; Levshin et al. 2010), is
7 a measure of the effect of local velocity and density structure beneath the receiver on the
8 observed surface wave amplitude. The fundamental physical principle underlying local
9 amplification is conservation of energy flux, where a wave traveling from a denser/faster
10 medium (high impedance) to a lighter/slower medium (low impedance) will undergo an
11 increase in amplitude. Similarly, a wave traveling from a lighter/slower medium (low
12 impedance) to a denser/faster medium (high impedance) will experience an amplitude
13 reduction. Theoretical studies (e.g. Tromp & Dahlen 1992) have shown that for a
14 smoothly varying earth model, where modal coupling can be ignored, the local
15 amplification can be determined if the 1D velocity and density profile is known directly
16 beneath the location (see Section 2). Conversely, the ability to measure the local
17 amplification would provide a direct constraint on the local velocity and density
18 structure. The measurement of surface wave velocity and amplification, therefore,
19 provides a hitherto unexploited constraint on density. Moreover, the ability to constrain
20 local amplification would also reduce bias in estimates of anelastic attenuation.
21 Analogous to studies based on the dispersion of phase and group velocity, the vertical
22 distribution of density may, in principle, be inferred by investigating the frequency
23 dependence of surface-wave amplification.

1 Because local amplification only affects the amplitude measurement at the station
2 location, traditional surface wave tomography studies (e.g. Dalton & Ekstrom 2006b)
3 based on a sparse station distribution could not resolve spatial variations in local
4 amplification. The existence of regional arrays such as USArray, on the other hand,
5 allows the amplification to be observed and inverted at the station locations together with
6 other surface wave parameters (e.g., Yang & Forsyth 2006a). To estimate the local
7 amplification accurately, the effects of both elastic focusing/defocusing and anelastic
8 attenuation must be accounted for properly in the surface wave amplitude measurements
9 (Dalton & Ekstrom 2006; Levshin et al. 2010). The situation is further complicated by the
10 practically indistinguishable nature of local amplification and variations in instrument
11 responses. To our knowledge, local amplification has not yet been used to study 3D
12 velocity and density structure.

13 Anelastic attenuation, on the other hand, describes the intrinsic decay of wave energy lost
14 to heat. The ability to estimate intrinsic anelastic attenuation at relatively high resolution
15 would probably improve our understanding of the temperature state of earth's interior
16 (e.g. Jackson et al. 2002). Detailed source, path, and receiver effects need to be accounted
17 for to constrain anelastic attenuation accurately based on surface waves (e.g. Dalton &
18 Ekstrom 2006b). While source effects can potentially be mitigated by studying regional
19 wave propagation (e.g. Yang & Forsyth 2006a), as in this study, detailed path and
20 receiver effects such as focusing/defocusing and location amplification are also extremely
21 important to account for. Recently, interest has been growing in constraining crustal
22 attenuation based on ambient noise cross-correlations (e.g. Prieto et al. 2009; Lawrence
23 & Prieto 2011; Lin et al. 2011b; Tsai 2011). At high frequencies, however, the effect of

1 elastic scattering may be more important and distinguishing scattering attenuation from
2 anelastic attenuation is challenging.

3 In this study, we show that high resolution local amplification and large-scale anelastic
4 attenuation maps can be reliably constructed empirically by examining the surface-wave
5 amplitude and phase travel-time measurements across USArray based on earthquake
6 data. In particular, similar to eikonal and Helmholtz tomography (Lin et al. 2009; Lin &
7 Ritzwoller 2011a), we apply spatial differential operators to the observed amplitude and
8 phase travel time fields to directly study the effect of focusing/defocusing, attenuation,
9 and local amplification. We use the Laplacian of phase travel time, which essentially
10 describes phase-front distortion, to account for the effects of focusing/defocusing. To
11 distinguish the effects of attenuation from amplification, measurements for waves coming
12 from different directions are compared. To validate the observed amplification maps, we
13 show that the maps are correlated with known velocity structures and generally agree
14 well with predictions based on realistic 3D velocity models constrained by phase-velocity
15 measurements alone. We suggest that several detailed discrepancies between the
16 predicted and observed amplification maps are at least partially due to inaccuracies in the
17 density model used. While the observed high-resolution attenuation maps are probably
18 biased by unmodeled surface wave phenomena near sharp structural boundaries, large-
19 scale attenuation maps appear to be well correlated with known tectonic features. More
20 specifically, the tectonically active western US and the eastern stable cratonic US are, as
21 expected, characterized by high and low anelastic attenuation, respectively.

22 Although we have applied the methods presented here to determine both local
23 amplification and anelastic attenuation for Rayleigh waves from 24 s to 100 s period

1 across the western US, only the results at 30 s and 60 s are presented to demonstrate the
 2 method. In principle, the same method can also be applied to Love waves. It is planned
 3 that the inversion for 3D velocity, density, and anelastic structure based on the local
 4 amplification and attenuation constrained here will be the subject of future contributions.

5 **2. Theoretical Background**

6 In this section, we derive the basic equations used to study Rayleigh-wave amplification
 7 and attenuation based on vertical-component measurements. While it is not presented
 8 here, a similar derivation can be performed for Love waves.

9 For a smoothly varying earth model, the single frequency 2D surface wave potential χ_{2D}
 10 approximately satisfies the 2D homogenous wave equation (Tanimoto 1990; Tromp &
 11 Dahlen 1993)

$$12 \quad \frac{1}{c(\mathbf{r})^2} \frac{\partial^2 \chi_{2D}(\mathbf{r}, t)}{\partial t^2} = -\frac{2\alpha(\mathbf{r})}{c(\mathbf{r})} \frac{\partial \chi_{2D}(\mathbf{r}, t)}{\partial t} + \nabla^2 \chi_{2D}(\mathbf{r}, t) \quad (1)$$

13 where c and α are the phase velocity and the attenuation coefficient, respectively, and \mathbf{r} is
 14 the position on the 2D surface. α is related to the attenuation quality factor Q by $\alpha =$
 15 $\pi f / CQ$, where C is the group velocity and f is the wave frequency (e.g. Prieto et al. 2009).
 16 Based on conservation of energy flux, Tromp & Dahlen (1992) showed that the 3D
 17 Rayleigh-wave vertical-component displacement wavefield observed on the surface, u_{3D} ,
 18 can be related to the 2D potential, χ_{2D} , through a local amplification factor, β , such that

$$19 \quad u_{3D}(\mathbf{r}, t) = A(\mathbf{r}) e^{i\omega[t - \tau(\mathbf{r})]} = \beta(\mathbf{r}) \chi_{2D}(\mathbf{r}, t) \quad (2)$$

1 where A and τ are the observed amplitude and phase travel time at frequency ω of the 3-
 2 D wavefield. The local amplification, β , can be expressed as

$$3 \quad \beta(\mathbf{r}) = \left(\frac{c(\mathbf{r})C(\mathbf{r})I_1(\mathbf{r})}{c'CI_1'} \right)^{-\frac{1}{2}} \quad (3)$$

4 where c is the phase velocity and I_1 is the depth integral of density ρ (from the center of
 5 the earth, $z=0$, to the surface, $z=a$) modulated by the normalized eigenfunctions beneath
 6 location \mathbf{r}

$$7 \quad I_1 = \int_0^a \rho(z) \left(U(z)^2 + V(z)^2 \right) z^2 dz. \quad (4)$$

8 U and V are the normalized eigenfunctions ($U(a)=1$) for Rayleigh waves in the vertical
 9 and horizontal directions, respectively. Note that the c' , C' , and I_1' in eq. (3) represent
 10 reference quantities based on an arbitrary 1D reference model and the amplification β
 11 defined here is dimensionless. This is different from the absolute amplification $(cCI_1)^{-1/2}$
 12 defined in [Tromp & Dahlen \(1992\)](#). Because of this, the 2D potential χ_{2D} used here has
 13 the same dimensions as displacement. While the absolute amplification factor $(cCI_1)^{-1/2}$
 14 may potentially be constrained when the absolute energy flux is known, such information
 15 is usually unavailable for regional studies based on teleseismic earthquakes. In this study,
 16 we will focus on resolving the spatial variation of the dimensionless amplification β .

17 Substituting the 2D wave potential from eq. (2)

$$18 \quad \chi_{2D}(r, t) = \frac{A(r)}{\beta(r)} e^{i\omega[t-\tau(r)]}$$

19 into eq. (1), the real-part of the resulting expression is

$$1 \quad \frac{1}{c^2} = \nabla \tau \cdot \nabla \tau - \frac{\nabla^2(A/\beta)}{\omega^2(A/\beta)}. \quad (5)$$

2 (For the sake of conciseness, we drop the dependency of all variables on r). Eq. (5) is the
 3 basic equation used in the Helmholtz tomography method (Lin & Ritzwoller 2011a), in
 4 which we previously assumed a constant amplification term ($\beta=1$). The gradient of travel
 5 time in eq. (5) gives the apparent phase slowness and, with the frequency dependence, the
 6 Laplacian term is a finite frequency correction of the apparent phase slowness
 7 measurement. For high frequency applications, the Laplacian term can be dropped and
 8 eq. (5) becomes the eikonal equation

$$9 \quad \frac{\hat{k}}{c} = \nabla \tau \quad (6)$$

10 where \hat{k} describes the direction of wave propagation. Eq. (6) is the basic equation used in
 11 eikonal tomography (Lin et al. 2009), which describes geometrical ray theory.

12 In contrast to equation (5), the imaginary-part of the resulting expression is

$$13 \quad -\frac{2\alpha}{c} = \frac{2\nabla(A/\beta) \cdot \nabla \tau}{A/\beta} + \nabla^2 \tau \quad (7)$$

14 in which the attenuation constant is seen to be related to the 2D amplitude decay in the
 15 direction of wave propagation (first term on the right hand side (RHS) of eq. (7))
 16 corrected by the Laplacian of the phase travel time field (second term on the RHS of eq.
 17 (7)). The Laplacian correction term here basically describes the curvature of the phase
 18 front that results from elastic focusing/defocusing. To investigate the local amplification
 19 β , the first term on the RHS of eq. (7) is expanded to give:

$$1 \quad \frac{2\nabla\beta \cdot \nabla\tau}{\beta} - \frac{2\alpha}{c} = \frac{2\nabla A \cdot \nabla\tau}{A} + \nabla^2\tau. \quad (8)$$

2 The RHS of eq. (8) contains only quantities that are directly measurable from the surface
 3 wavefield (A, τ) of a single-frequency vertical-component Rayleigh wave on the earth's
 4 surface. The unmeasurable quantities that we wish to infer (c, β, α) appear exclusively on
 5 the left hand side (LHS), although we may assume that phase speed c has been locally
 6 estimated based on the real-part expression, eq. (5) or (6). There are, therefore, two
 7 remaining unknowns: local amplification β appears only in the first term on the LHS and
 8 the attenuation coefficient α only in the second term on the LHS.

9 We refer here to the first term on the RHS of eq. (8) as the “apparent amplitude decay”
 10 (in the direction of wave propagation). The combination of both terms on the RHS is
 11 referred to as the “corrected amplitude decay”, where the Laplacian of the travel time
 12 field provides the correction for focusing and defocusing. On the LHS of eq. (8), the first
 13 term is referred to as the local “amplification term” for the Rayleigh wavefield. There is,
 14 therefore, a potential terminological confusion between the local amplification β , which
 15 is a property of the Rayleigh wave, and the amplification term, which is a mathematical
 16 construct. The second term on the LHS is the “anelastic attenuation” term.

17 Thus, from eq. (8) it is clear that the corrected amplitude decay will differ from the
 18 anelastic attenuation term by the local amplification term. However, the amplification
 19 term on the LHS contains the gradient of the phase travel time and will vary with the
 20 direction of wave propagation whereas the attenuation term is azimuth-independent. In
 21 the approach described below, we attempt to separate the effect of attenuation and

1 amplification by examining the directional-dependence of the corrected amplitude decay
2 measurements.

3 **3. Method**

4 We closely follow the method described by [Lin et al. \(2009\)](#) and [Lin & Ritzwoller](#)
5 [\(2011a\)](#) to select the data and construct both phase travel time and amplitude maps across
6 USArray Transportable Array. More than 900 earthquakes ([Fig. 1b](#)) with $M_s > 5.0$ between
7 2007 January 1 and 2011 June 30 are used. An example of the observed 60-sec Rayleigh-
8 wave phase travel time and amplitude maps for a 2009 Kuril Islands earthquake is shown
9 in [Figure 2](#). Unlike phase travel time measurements, which mostly increase
10 monotonically in the direction of wave propagation, the observed amplitude
11 measurements often vary in both radial and transverse directions due to the combination
12 of interference, focusing/defocusing, attenuation, and amplification effects. The striping
13 pattern in [Figure 2b](#), for example, is probably due to the interference between waves
14 coming from the continental and oceanic flanks of the great circle path. In this section,
15 we will use 60-sec Rayleigh wave measurements, which are most sensitive to uppermost
16 mantle structure, to demonstrate our method.

17 **3.1 Corrected amplitude decay measurement**

18 We now demonstrate the ability to correct for amplitude variations in the direction of
19 wave propagation caused by elastic focusing/defocusing. [Figures 3a-b](#) compare the
20 apparent amplitude decay ($2\nabla A \cdot \nabla \tau / A$) and the focusing/defocusing correction ($\nabla^2 \tau$)
21 derived from the amplitude and travel time measurements presented [Figure 2](#). Our
22 method here differs somewhat from the presentation of [Lin & Ritzwoller \(2011a\)](#), in that

1 here we utilize Gauss' theorem to estimate the Laplacian of phase travel time by
2 performing a contour integral in the gradient of phase travel time. For each location, the
3 contour is defined on the boundary of a $1.2^\circ \times 1.2^\circ$ box centered at that point. In an
4 attempt to match the resolution between gradient and Laplacian operators, the apparent
5 amplitude decay is also estimated based on the average value within the same box. A
6 clear anti-correlation is observed between the apparent amplitude decay and the
7 focusing/defocusing correction shown in Fig. 3a-c, as suggested by eq. (8). Note that the
8 same Kuril Island earthquake is also used by Lin & Ritzwoller (2011a) to demonstrate the
9 principle of Helmholtz tomography and is compared with eq. (5). By removing the
10 focusing/defocusing effect, the corrected amplitude decay (Fig. 3d) eliminates the
11 apparent striping bias and is better correlated with the boundaries of known velocity
12 structures (Fig. 4). For example, strong amplitude decay (red) in western Wyoming is
13 coincident with the boundary between the Yellowstone/Snake River Plain slow anomaly
14 and the southwestern Wyoming fast anomaly. The increase of amplitude (blue) in
15 western Colorado, on the other hand, is coincident with the boundary between the
16 Colorado Plateau/southwestern Wyoming fast anomalies and the southern Rockies slow
17 anomaly. The fact that the corrected amplitude decay map (Fig. 3d) is well correlated
18 with the observed velocity boundaries, however, suggests that the corrected amplitude
19 decay actually is dominantly affected by local amplification rather than anelastic
20 attenuation. The local amplification β is expected to correlate with velocity structure as
21 shown in eq. (3).

22 Due to the dependence of the amplification factor on the phase travel time gradient (eq.
23 8), the observed corrected amplitude decay is expected to vary with wave propagation

1 direction. In **Figure 5**, we examine measurements with waves propagating in two primary
2 directional bands: southeast (120° to 150° azimuth; **Fig 5a-c**) and northwest (300° to 330°
3 azimuth; **Fig 5d-f**), where the amplification terms are expected to have exactly opposite
4 effects. More than 80 earthquakes are averaged in each of the two azimuthal bands. As in
5 previous studies (**Lin et al. 2009; Lin & Ritzwoller 2011a**), the direction of wave
6 propagation for each earthquake at each location is determined from the gradient of phase
7 travel time (eq. 6). In the overlapping region, the average apparent amplitude decay,
8 focusing/defocusing correction, and corrected amplitude decay for waves coming from
9 the northwest (**Fig 5a-c**) are largely consistent with the Kuril island earthquake
10 measurements (**Fig. 3**). Anti-correlation between the apparent amplitude decay and the
11 focusing/defocusing correction is again observed for both directions (**Fig. 4a-b, d-e**),
12 particularly where the focusing/defocusing correction is strong. Clear anti-correlation can
13 also be observed for the corrected amplitude decay for the two opposite directions (**Fig.**
14 **5c and 5f**), which suggests that not only is eq. (8) valid but also that the amplification
15 effect is much stronger than the variation of anelastic attenuation at this period. Note that,
16 in principle, the focusing/defocusing effect can also be used to determine velocity
17 structure variations. However, this is beyond the scope of this study.

18 **3.2 Amplification map**

19 To determine the amplification effect accurately, the effect of attenuation must be
20 removed from the corrected amplitude decay measurements. We do this by studying the
21 directional dependence of the measurements. With the dot product in the amplification
22 factor (eq. 8), we expect the observed corrected amplitude decay to have a 360°
23 azimuthal periodicity at each location where the variation should be independent from

1 attenuation. An example of observed directionally-dependent corrected amplitude decay
2 measurements at a point near western Wyoming (star in Fig. 1a) is shown in Figure 6a.
3 Here, similar to previous studies on the directional-dependence of phase velocity
4 measurements (Lin et al. 2009; Lin et al. 2011a; Lin & Ritzwoller 2011a; Lin &
5 Ritzwoller 2011b), the mean and the standard deviation of the mean for all available
6 measurements within each 20° azimuthal bin are used to estimate the corrected amplitude
7 decay and its uncertainty for each direction. Note that the 9-point (3 by 3 grid with 0.6°
8 spacing) spatial averaging scheme described by Lin et al. (2009) is applied here to reduce
9 the uncertainty for each measurement, but it also degrades the resolution to ~200 km. A
10 clear 360° azimuthal periodicity is observed in Figure 6a, where a large positive
11 amplitude decay is associated with waves propagating toward the northwest (from the
12 southwestern Wyoming fast anomaly into the Yellowstone/Snake River Plain slow
13 anomaly) and a negative amplitude decay (or amplification) is associated with waves
14 propagating in the opposite direction.

15 Based on the observation of the directionally-dependence of such measurements (e.g.,
16 Figure 6a), we fit a single sine-function with 360° periodicity to the corrected amplitude
17 decay measurements at each location to estimate both the maximum amplification
18 direction and the amplification amplitude. We associate these two parameters with the 2D
19 vector $2\nabla\beta|\nabla\tau|/\beta$ based on eq. (8). Because the anelasticity term is not directionally
20 dependent, the mean of the sine function can be used to estimate the attenuation factor α .
21 This will be the subject of further discussion in section 5. The observed amplification
22 amplitudes for the 60-sec Rayleigh waves across the whole array are summarized in
23 Figure 6b, where the maximum amplification directions are also plotted where the

1 amplification amplitudes are large ($>0.15 \cdot 10^{-3} \text{ sec/km}^2$). As expected, large amplification
 2 amplitude is observed near sharp velocity structural boundaries (Figure 4) with maximum
 3 amplification directions pointing toward the slow anomalies (e.g. Yellowstone/Snake
 4 River Plain and Southern Rockies). Note that a very similar pattern is observed for the 1ψ
 5 (360° periodicity) azimuthally anisotropic phase velocity measurements. This apparent
 6 bias has been attributed to finite-frequency sensitivity to backscattering (Lin &
 7 Ritzwoller 2011b).

8 By approximating the phase slowness $1/c$ as the absolute value of the apparent slowness
 9 $|\nabla\tau|$ and using the phase velocity map derived from Helmholtz tomography, we now have
 10 an estimate of the normalized amplification gradient vector field $\nabla\beta/\beta$. Because this
 11 vector field is essentially derived from the amplification differences observed between
 12 nearby stations, we invert the amplification β_i at each station location based on this vector
 13 field by minimizing the misfit functional

$$14 \quad \text{misfit} = \sum_{i,j} \left[\frac{2(\beta_j - \beta_i)}{(\beta_j + \beta_i)} - \frac{\nabla\beta}{\beta} \Big|_{\frac{(\mathbf{r}_i + \mathbf{r}_j)}{2}} \cdot (\mathbf{r}_j - \mathbf{r}_i) \right]^2 \quad \forall \quad |\mathbf{r}_j - \mathbf{r}_i| < 120\text{km} \quad (9)$$

15 where i, j are the station indices, \mathbf{r} is the station location, and $(\mathbf{r}_i + \mathbf{r}_j)/2$ is the mid-point
 16 between station pair (i, j) where the normalized amplification gradient vector is
 17 evaluated. In order only to evaluate the closest station pairs that contribute to the
 18 observed amplification gradient vector field, the summation is taken over all station pairs
 19 that are within 120 km of one another. To obtain a unique solution, we set the average
 20 amplification of all stations to be 1 by using the freedom of selecting an arbitrarily
 21 reference model in eq. (3). Also, to linearize the inversion we assume that the variation of

1 amplification is small such that $(\beta_i + \beta_j)/2$ is approximately equal to 1. The inverted
2 amplification map based on the maximum amplification directions and amplification
3 amplitudes shown in [Figure 6b](#) and eq. (9) is shown in [Figure 7a](#), where we interpolate
4 the result to cover the whole area based on the minimum curvature surface-fitting method
5 ([Smith & Wessel 1990](#)).

6 The amplification map for the 60-sec Rayleigh wave ([Fig. 7a](#)) is consistent with
7 expectations based on eq. (3) where high and low amplifications are associated with slow
8 and fast phase speed anomalies ([Fig. 4](#)), respectively. For example, in regions like the
9 Southern Rockies and the Yellowstone/Snake River Plain slow anomalies, slowly
10 propagating waves are associated with large amplifications in order to satisfy the
11 conservation of energy flux. Potential bias in this inversion can be reduced by an iterative
12 process. In each iteration, we use the inverted station amplification β to remove the
13 amplification effect from the raw amplitude measurement and re-evaluate the remnant
14 amplification based on the updated corrected amplitude decay measurements. Because
15 the remnant amplification at each station is now closer to 1, the error in the inversion is
16 reduced. The remnant amplification is then used to correct for the original amplification.
17 [Figures 7b](#) and [7c](#) show the amplification maps after the second and third iteration,
18 respectively. In general, the small-scale amplification anomalies become more
19 pronounced upon each iteration, but the result converges quickly. Hereafter, we use the
20 amplification map produced after three iterations as the final result.

21 A synthetic test based on 2D simulations has been performed to validate the method
22 described here and the result is presented in the appendix section. While 3D wave
23 phenomena, such as mode coupling, are not considered in the 2D simulations, the

1 synthetic test clearly demonstrates the ability of using our method to account for 2D wave
2 phenomena, such as focusing/defocusing, and to accurately reconstruct the theoretical
3 local amplification.

4 **4. Observed amplification compared with amplification computed from 3-D models**

5 In the previous section, we described a method to construct amplification maps for
6 surface waves empirically based on maps of surface wave phase travel time and
7 amplitude. In this section, we validate these maps and demonstrate the potential of
8 incorporating the amplification information into 3D inversions for shear velocity and
9 density. We perform this validation by comparing the observed 30- and 60-sec Rayleigh
10 wave amplification with predictions based on two 3D shear velocity models in the
11 western US. The two models have both been constructed based on Rayleigh wave phase
12 velocity measurements and are only different in how the density model is prescribed. The
13 30- and 60-sec Rayleigh waves are most sensitive to the lower crust/uppermost mantle
14 and the upper mantle, respectively.

15 We use a method similar to that described by [Yang et al. \(2008\)](#), who inverted for a 3D
16 shear velocity model based on Rayleigh wave phase velocity maps observed between 8
17 and 100 sec period. The phase velocity maps used here are constructed based on eikonal
18 and Helmholtz tomography for ambient noise (8 to 24 sec) and earthquake (24 to 100
19 sec) datasets, respectively ([Lin et al. 2008](#); [Lin et al. 2009](#); [Lin & Ritzwoller 2011a](#)).

20 Note that the estimated amplification map allows for a reevaluation of the earlier result of
21 Helmholtz tomography based on eq. (5). Only the small-scale anomalies are slightly
22 different from the previous application ([Lin & Ritzwoller 2011a](#)), where a constant

1 amplification term β is assumed. At each point, the 1D shear velocity profile from the
2 surface to 200 km depth is described by six quadratic B-splines, three in the crust and
3 three in the upper mantle. A velocity discontinuity is allowed between the crust and upper
4 mantle where we fix the Moho depth based on previous receiver function studies (Gilbert
5 & Flesch 2009). We set the V_p/V_s ratio to 1.78 in both the crust and the upper mantle. In
6 the first model (Model I), we assume a non-realistic homogeneous density model where
7 the crust and mantle have the same density everywhere (3 g/cm^3). In the second model
8 (Model II), we assume a more realistic density model where crust and mantle densities
9 are uniform but differ by $\sim 20\%$ across the Moho (crust: 2.7 g/cm^3 ; mantle: 3.38 g/cm^3).
10 Both models fit the observed phase velocity dispersion curves acceptably (within errors)
11 and the shear velocity structure, in general, is very similar to that presented by Moschetti
12 et al. (2010b) and Lin et al. (2011a).

13 **4.1 60-sec Rayleigh waves**

14 For each location, with the 1D velocity and density models defined in the previous
15 paragraph, all terms in eq. (3) can be calculated and the amplification can be predicted.
16 Figure 8 shows a comparison between observed and predicted amplification maps for the
17 60-sec Rayleigh wave. Note that the area of our 3D inversion is confined to the region
18 with reliable constraints on Moho depth (Gilbert & Flesch 2009) and the amplification
19 maps are all normalized to the mean amplification in the area. The observed amplification
20 maps shown in Figure 8a, therefore, are slightly different from Figure 7c due to the
21 different area covered.

1 The pattern of observed amplification (Fig. 8a) generally agrees well with the predicted
2 amplification (Fig. 8b-e). This validates both the observed amplification map and the
3 assumption that it can be predicted from eq. (3). The differences between the predicted
4 maps based on the two different density models are generally small. This is probably due
5 to the insensitivity of 60-sec Rayleigh waves to density variations near the Moho. The
6 sensitivity peaks around 90 km depth for 60-sec Rayleigh-wave phase velocity (see
7 section 5.2), compared to a Moho depth that is on average shallower than 40 km across
8 our study area (Gilbert & Flesch 2009).

9 Despite the general agreement between the observed and predicted amplification, detailed
10 discrepancies are apparent. First, the variation of amplification is generally under-
11 predicted by the 3D models. Aside from small-scale features, which can simply be due to
12 inconsistent resolution between the models and the amplification map, a long wavelength
13 discrepancy is observed where stronger than predicted amplification appears in the
14 tectonically active western US and weaker than predicted amplification appears in the
15 tectonic more stable eastern US. While there are several possibilities that will be the
16 subject of a future study, simply allowing for a more buoyant upper mantle in the western
17 US will produce a slightly stronger amplification in the west and reduce this long
18 wavelength discrepancy. This would be consistent with the assumption of a hot and
19 buoyant upper mantle in the tectonically active western US (e.g. Lowry et al. 2000).
20 Second, we observe a distinguishable cluster of points in the prediction versus
21 observation scatter plots (Fig. 8d-e) with weak observed amplification (<1) and strong
22 predicted amplification (>1). Intriguingly, these points mostly correspond to the area near
23 the northwestern Pacific coast where the Juan de Fuca Plate is currently subducting

1 beneath the North American Plate. While uncertainties are expected to be higher near to
2 the edge of the station coverage, allowing for denser mantle within the slab would
3 suppress the local amplification and again reduce the discrepancy.

4 It must be acknowledged that while density structure can certainly affect the
5 amplification, as suggested by eq. (3), variations in velocity structure are still likely to
6 have a dominating effect. Considering that velocity and density structures are frequently
7 correlated, it will prove difficult to recover the density effect without an accurate 3D
8 velocity model.

9 **4.2 30-sec Rayleigh waves**

10 Rayleigh waves of 30 sec period, in which the peak phase sensitivity lies near 45 km
11 depth (see section 6), are expected to be more sensitive to structural variations near the
12 Moho than the 60 sec period waves. **Figure 9** shows the comparison between the
13 observed and predicted amplification maps for 30-sec Rayleigh waves in the western US.
14 Again, we see a broad agreement between the observed amplification and the predictions
15 based on the 3D models based on the two different density structures. The fact that even
16 the prediction based on a non-realistic density model agrees fairly well with the
17 observation suggests that the observed amplification is dominantly controlled by velocity
18 structure.

19 A detailed comparison, however, shows that the variation in amplification is somewhat
20 underpredicted for the homogeneous density model (**Fig. 9b,d**). Regions with strong
21 amplification (>1.1), such as the southern Rockies, present a stronger than predicted
22 amplification and regions with weak amplification (<0.9), such as the Columbia Basin

1 and the Salton Trough, present a weaker than predicted amplification. These strong and
2 weak amplification regions generally correspond to regions with high and low
3 topography, respectively. They also generally correspond to regions with thick and thin
4 crust, respectively, as observed by receiver function studies (e.g. Gilbert & Flesch 2009).
5 In either case, it is reasonable to hypothesize that the stronger and weaker than predicted
6 amplifications are, at least in part, due to differences that are not accounted for in our
7 homogeneous density model.

8 Further information about the role of density in predicting amplification comes from the
9 second density model that has a more realistic ~20% density jump across the Moho. The
10 agreement between the observed and predicted amplification, in general, is better than
11 with the vertically homogeneous density model (Fig. 9c,e). The southern Rockies, for
12 example, still have a slightly underpredicted amplification, but the discrepancy is smaller.
13 Although the Salton Trough and adjacent regions appear to be overcorrected, we do see
14 that most weak amplification regions (<0.9) have better agreement between the
15 predictions and observations. Note that a large discrepancy is observed near the coast in
16 the Pacific northwest. However, both the velocity model and amplification map may not
17 be accurate near the edge of the station coverage. While more tests remain to be
18 completed, we consider these comparisons to be an encouraging first step towards
19 potential velocity and density tomography involving surface wave amplification.

20 **5. Attenuation map**

21 To this point we have concentrated on the observation of local amplification, but
22 attenuation structure can also be estimated based on this method. From eq. (8), we may

1 also estimate the attenuation term $-2\alpha/c$, but it will be necessary to correct for the
2 amplification term. One method would be to compute the amplification term by using the
3 amplitude map discussed above. However, we can also exploit the fact that the
4 amplification term is azimuthally variable whereas the anelastic attenuation term is not.
5 Thus, by averaging the corrected amplitude decay measurements over azimuth, we can
6 effectively cancel the amplification effect. To avoid bias due to an uneven source
7 distribution, the weight for each measurement is equated with the reciprocal of the
8 number of measurements within each 25° azimuthal bin. By averaging the measurements
9 at a particular location over azimuth, the first term on the LHS of eq. (8) will
10 approximately cancel and the corrected amplitude decay (RHS of eq. (8)) will
11 approximate the anelastic attenuation term ($-2\alpha/c$). Alternately, attenuation constants
12 could be estimated from the fit of the 360° -periodicity sine function described in section
13 3.2, but the results are very similar to those presented here.

14 Because the effect of anelastic attenuation in our amplitude decay measurements is
15 relatively small (e.g. Fig. 6a), high-resolution attenuation maps may be more easily
16 biased by details of wave propagation caused by elastic inhomogeneities. Here, we
17 examine large-scale attenuation structure, which should be more accurate and reliable.
18 For each location, we first determine the weighted azimuthal average of corrected
19 amplitude decay. The average value over a 4° radius circle is used to estimate large-scale
20 attenuation structure ($-2\alpha/c$), and the results at periods of 30 s and 60 s are summarized in
21 Figure 10. The attenuation quality factor Q may be roughly estimated by approximating
22 the phase and group velocities for 30 s Rayleigh waves as 3.7 km/s and 3.2 km/s,
23 respectively, and 3.85 km/s and 3.6 km/s for 60 s Rayleigh waves (Fig. 10). At 30 sec

1 period, Rayleigh waves are most sensitive to uppermost mantle structure. Clear structural
2 differences are observed between the tectonically active western US and the stable
3 cratonic eastern US where the presumable hotter crust and uppermost mantle in the west
4 is characterized by a higher attenuation and lower Q. More specifically, the largest
5 values of attenuation are observed beneath the High Lava Plains, the Snake River
6 Plain/Yellowstone hot spot track, and the Southern Rockies where significant low shear
7 velocities are also observed (Fig. 4; Lin et al. 2011a). Note that the anomalous low and
8 high attenuations near the northwestern and southeastern corners, respectively, are near
9 the edge of the station coverage and are probably less reliable.

10 The 60 sec results for Rayleigh waves are most sensitive to structure between 50 and 150
11 km depth and are shown in Figure 10b. Clear structural differences between the
12 tectonically active western US and the more stable cratonic eastern US are again
13 apparent. While 60-sec Rayleigh waves are sensitive to the asthenosphere in the western
14 US, they are only sensitive to the lithospheric layer in the east. This result also generally
15 agrees with previous, lower resolution (>1000 km), global studies (e.g. Dalton &
16 Ekstrom 2006b). Perhaps more surprising is the observation of the largest attenuations
17 between the Colorado Plateau and areas near the Pacific coast where fast anomalies are
18 observed in the phase velocity map (Fig. 4b). In these areas, the fast anomalies are
19 surrounded by slow anomalies where energy loss due to elastic scattering may be
20 important.

21 To understand the potential biases introduced by complex wave phenomena, the high-
22 resolution (without 4° averaging) weighted average over azimuth of the apparent
23 amplitude decay (first term on the RHS of eq. (8)), the focusing/defocusing correction

1 (second term on the RHS of eq. (8)), and corrected amplitude decay measurements (entire
2 RHS of eq. (8)) for the 60-sec Rayleigh wave are presented in **Figure 11**. The azimuthally
3 averaged effect of focusing/defocusing (**Fig. 11b**) is strongly correlated with the phase
4 velocity structure (**Fig. 4**) and with the azimuthally averaged apparent amplitude decay
5 (**Fig. 11a**). The apparent amplitude decay, therefore, is clearly biased by wavefield effects
6 that result from nearby elastic inhomogeneities and should not be used directly to
7 evaluate the attenuation, even when measurements from all azimuths are available. In
8 fact, the focusing/defocusing correction term is of the same order of magnitude as the
9 apparent decay term and the corrected amplitude decay results from a relatively fine
10 cancellation between these two observables. Thus, it is perhaps not surprising that the
11 corrected amplitude decay map (**Fig. 11c**), while mostly showing negative values
12 consistent with the expectation of a positive attenuation constant α , does not display
13 strong geological coherence. For example, the Yellowstone/Snake River Plain low
14 velocity anomaly probably reflects warm mantle temperatures and is expected to be
15 strongly attenuating. Also, the Colorado Plateau high velocity anomaly is probably cold
16 and weakly attenuating in the mantle. Thus, at present this method appears to have
17 trouble resolving high-resolution attenuation structure. One reason for this may be
18 because the amplitude of the focusing/defocusing correction is relatively poorly
19 constrained at smaller scales and the fine cancellation between the apparent amplitude
20 decay and the correction term is insufficiently accurate to recover high-resolution
21 information about attenuation. The fact that large-scale attenuation at 60 sec period (**Fig.**
22 **10b**) appears to retain some of the biases observed for the high-resolution result (**Fig.**

1 11c), but does not at 30 sec, suggests that the biases are probably due to finite frequency
2 effects which are stronger at longer periods.

3 In addition to difficulties in estimating the amplitude of the focusing/defocusing
4 correction term at small-scales, we believe that more subtle 3D wave phenomena may
5 exist that are not accounted for within the 2D framework of our analysis and may further
6 worsen our estimates of attenuation. If we compare the corrected amplitude decay
7 measurements observed in Figure 5c and 5f in detail, we find that while the patterns are
8 generally anti-correlated for waves propagating in opposite directions, the locations of
9 some of the prominent features do not match perfectly in the two maps. For example,
10 near the boundary of the Snake River Plain low velocity anomaly and the southwestern
11 Wyoming high velocity anomaly, the significant amplitude decay for waves heading
12 southeast is located southeast of the significant amplitude increase for waves heading
13 northwest. Assuming that these features are solely due to the amplification effect across
14 the velocity structure boundary and the 2D approximation discussed in section 2 is
15 correct, we would expect them to be nearly exactly co-located in the two maps (Fig. 5c
16 and 5f). The apparent shift of these features as a function of the direction of wave
17 propagation potentially represents the breakdown of the 2D approximation and suggests
18 leakage of the amplification effect into the observed attenuation structure. In fact, Yang
19 & Forsyth (2006b) have shown through a numerical simulation that the amplification
20 effect due to a sharp structural boundary only gradually approaches its 2D theoretical
21 prediction after the simulated Rayleigh wave passes the boundary. Because the
22 amplification effect is much larger than the attenuation effect for local measurements, the

1 details of this apparent shift need to be understood before high-resolution attenuation
2 tomography can be performed reliably.

3 **6 Structural sensitivity of local amplification**

4 In this section we compare the depth sensitivity kernels of local amplification with other
5 types of 2D surface wave quantities such as phase velocity, group velocity, and the I_1
6 integral defined in eq. (4). The I_1 quantity is included here because it can be estimated
7 based on eq. (3) when phase velocity, group velocity, and amplification have all been
8 measured locally. Here we use the 1D PREM earth model (Dziewonski & Anderson
9 1981) as the reference model and compute the depth sensitivity kernels numerically by
10 perturbing the model. The 2D surface wave quantities for any given 1D model are
11 calculated using the code developed by Herrmann & Ammon (2004). Figure 12
12 summarizes the sensitivity kernels for the 30- and 60-sec Rayleigh waves due to
13 perturbations in compressional velocity (V_p), shear velocity (V_s), and density (ρ). While
14 the surface wave attenuation ($1/Q$) kernels are not shown here, they are very similar to
15 the phase velocity kernels by replacing the shear and compressional velocity
16 perturbations (V_s and V_p) by shear and compressional anelastic perturbations ($1/Q_s$ and
17 $1/Q_p$), respectively (Dalton et al. 2008).

18 The phase and group velocities, which are the observables for most traditional surface
19 wave tomography, are clearly dominantly sensitive to shear velocity (V_s) structure with
20 longer period Rayleigh waves more sensitive to deeper structure (Fig. 12a-b, e-f). While
21 velocity measurements are also affected by V_p and density, the generally weaker
22 sensitivity and potential tradeoff often prevent them from being estimated simultaneously

1 with V_s . The I_1 integral and the local amplification sensitivity kernels, on the other hand,
2 are different from phase and group velocity sensitivity kernels in a few distinguishing
3 ways (Fig. 12c-d, g-h). First, unlike phase and group velocities, the sensitivities to V_p
4 and V_s perturbations have opposite signs at shallow depths. While a fast V_p perturbation
5 near the surface reduces the amplification, a fast V_s perturbation intensifies the
6 amplification effect. Due to this opposing effect, the shallow V_p/V_s ratio may potentially
7 be better studied based on amplification measurements. Second, the density structure has
8 a relatively stronger effect on amplification than on phase and group velocities. This is
9 particularly true for the quantity I_1 (Fig. 12c, g) when both phase and group velocity can
10 be independently constrained. Hence, we believe that the ability to constrain local
11 amplification across a wide range of frequencies along with dispersive phase and group
12 velocity measurements will be the key to studying 3D density structure. Third, while the
13 local amplification is still strongly affected by shear wave perturbations, the amplification
14 kernels due to shear wave perturbations, unlike phase and group velocity kernels, have
15 three zero crossings. This makes the local amplification more sensitive to rapid shear
16 velocity variations with depth than group and phase velocities. Due to the broad depth
17 sensitivity kernel, traditional 1D inversion methods based on phase and group velocity
18 dispersion curves alone often suffer from the tradeoff between structures at nearby
19 depths. This tradeoff and the non-uniqueness of the inversion problem may potentially be
20 mitigated by jointly inverting the period dependence of both phase and group velocities
21 and amplification measurements.

22 While the ability to determine local amplification promises to provide new constraints on
23 3D variations in crustal and upper mantle structure, it should be remembered that the

1 local amplification determined based on our method is only a relative quantity. The fact
2 that the mean amplification over an area is arbitrary means that the observed
3 amplification cannot be used to invert independently for 1D structure at each location.
4 The comparison between the observed and predicted amplifications is only meaningful
5 when laterals variation are considered (e.g. [Fig. 8 & 9](#)).

6 With Rayleigh waves sensitive to compressional velocity, shear velocity, and density, it
7 is desirable to have three independent types of measurements to resolve the model
8 tradeoffs and non-uniqueness. Because the group velocity dispersion, in theory, can be
9 derived from the phase velocity dispersion, the phase velocity and amplification alone
10 only provide two independent types of constraints. The H/V ratio (e.g. [Tanimoto &](#)
11 [Rivera 2008](#)), or ellipticity, of Rayleigh waves, which describes the amplitude ratio
12 between radial (H) and vertical (V) component particle motion, is another independent
13 2D quantity that potentially may be used in a joint inversion. Initial attempts to determine
14 H/V ratios across USArray have shown clear correlations with known geological features
15 in the western US ([Lin & Tsai, in preparation](#)). Unlike Rayleigh waves, however, Love
16 waves are only sensitive to shear velocity and density structure and the inversion based
17 on Love wave velocity and amplification measurements may avoid the trade-off due to
18 variations in compressional velocity. While Rayleigh and Love waves are primarily
19 sensitive to vertically and horizontally polarized shear waves, respectively, which can be
20 different in the presence of radial anisotropy ([Moschetti et al. 2010a](#)), they are both
21 sensitive to the same density structure.

22 **7. Conclusions**

1 In this study, we present an empirical method to construct surface-wave amplification
2 and large-scale attenuation maps across a large array using the phase travel time and
3 amplitude maps observed across the array. The method utilizes spatial differential
4 operators to first determine the local amplitude variation and the focusing/defocusing
5 correction and then separates the amplification and attenuation effects by examining the
6 directional-dependence of the amplitude decay measurements.

7 The ability to construct surface-wave amplification maps may lead to not only new and
8 unique constraints on 3D velocity and density structure but also smaller bias in phase
9 velocity and attenuation measurements. Partly due to the traditional sparse station
10 configuration and perhaps partly due to the presumed larger uncertainties in amplitude
11 instrument responses, surface-wave amplification information has not been used in the
12 past as often as phase information. Here, we demonstrate that the amplification maps that
13 we construct across USArray not only correlate well with known major tectonic features
14 in the area but also compare well with predictions based on realistic 3D velocity models.
15 There are discrepancies, however, between the observed and predicted amplifications,
16 which may indicate errors in our 3D models. While the errors may be in the velocity
17 model, density model, or more likely both, the discrepancies can be mitigated by
18 constructing a more realistic density model. In particular, we show that without a density
19 jump between the crust and mantle across the Moho, the predicted amplification cannot
20 explain the 30-sec Rayleigh wave amplification in regions such as the Southern Rockies
21 and the Columbia Basin where the crust is anomalously thick and thin, respectively.

22 The large-scale attenuation maps, which clearly separates the highly attenuative
23 tectonically active western US from the less attenuative stable cratonic eastern US, are

1 probably useful in studying long-wavelength crustal and upper mantle temperature
2 structure. For the 30 sec Rayleigh wave, the observed attenuation also agrees well with
3 several known geological features if strong attenuation is observed in regions
4 characterized by high temperatures. Detailed attenuation structure at longer periods may
5 be more biased because of the smaller effect of anelastic attenuation on the observed
6 amplitude variations compared to other effects such as amplification and
7 focusing/defocusing from elastic inhomogeneities. While the effects of detailed 3D wave
8 phenomena on amplification and attenuation measurements remain to be understood, we
9 anticipate that this will be resolved based on numerical studies in the not too distant
10 future.

11 The natural extension of this study is to perform a 3D velocity, density, and anelasticity
12 inversion based on the observed phase velocity, amplification, and attenuation
13 measurements across a broad range of periods. To obtain a better constraint on crustal
14 structure, the amplification and attenuation information within the microseism period
15 band (5-20 sec) is desired. One of the technical challenges is to develop reliable means to
16 extract amplitude information from ambient noise cross-correlations (Tsai 2011; Lin et al.
17 2011b). We are optimistic that this development, along with the potential for a joint
18 inversion involving H/V ratio of Rayleigh waves, Love wave measurements, and body
19 wave measurements, will allow for detailed and unique crustal and upper mantle structure
20 to be resolved.

21 **Appendix (2D Synthetic test)**

1 In this section, we use the 2D finite difference method to simulate 60-sec Rayleigh waves
2 coming from eight different directions (Fig. A1) and test the method for constructing
3 amplification maps that we present here. For simplicity, we perform the simulations in
4 Cartesian coordinates where 1° longitude and latitude are both set equal to 100 km. For
5 each simulation, we solve the 2D wave equation for an inhomogeneous medium

$$6 \quad \frac{\partial^2 u_{2D}(\mathbf{r}, t)}{\partial t^2} = \nabla \cdot [c^2(\mathbf{r}) \nabla u_{2D}(\mathbf{r}, t)] \quad (\text{A1})$$

7 where c is the phase speed and c^2 can be considered to be the effective shear modulus
8 (with a constant density equal to 1). We introduce no attenuation in order to focus
9 exclusively on the amplification effect. While the 2D simulation does not fully account
10 for 3D surface wave propagation and will not reproduce the empirical observations, the
11 simulation does result in semi-realistic amplification due to the conservation of 2D
12 energy flux. We use the 60-sec Rayleigh wave phase velocity map from Helmholtz
13 tomography derived by Lin & Ritzwoller (2011a) as the reference model where
14 smoothing is applied outside of the array to cover the entire simulation area (Fig.A1). To
15 obtain a single frequency wave, we use a harmonic oscillating source in each simulation
16 and obtain both synthetic phase travel time and synthetic amplitude measurements across
17 the array. Figure. A2 shows an example of synthetic phase travel time and amplitude
18 maps constructed for two simulations with waves propagating in the southeast and
19 northwest directions, respectively.

20 Similar to the derivation shown in section 2, if we substitute the single frequency
21 expression of the 2D wavefield, $u_{2D}=A \exp[i\omega(t-\tau)]$, into eq. A1, the imaginary part of the
22 solution can be expressed as

1
$$\frac{2\nabla(1/c) \cdot \nabla\tau}{(1/c)} = \frac{2\nabla A \cdot \nabla\tau}{A} + \nabla^2\tau. \quad (\text{A2})$$

2 Eq. (A2) can be directly compared with eq. (8). We see that the role of the local
3 amplification β is played in this simulation by the inverse of phase velocity c .

4 We apply the same processes as described in section 3 to account for focusing/defocusing
5 and construct the amplification map based on the synthetic measurements. [Figure A3](#)
6 shows examples of the apparent amplitude decay (first term on the RHS of eq. (A2)), the
7 focusing/defocusing correction term (second term on the RHS of eq. (A2)), and the
8 corrected amplitude decay (the entire RHS of eq. (A2)) derived from the synthetic
9 measurements shown in [Figure A2](#) for waves coming from the northwest and southeast
10 directions. Similar to the results shown in [Figure 5](#), clear anti-correlations can again be
11 observed between the apparent amplitude decay and focusing/defocusing correction maps
12 for both of the directions ([Fig. A3a-b, d-e](#)). Clear anti-correlation can also be observed in
13 the corrected amplitude decay maps for waves propagating in the two opposite directions
14 ([Fig. A3c, f](#)). The pattern of corrected amplitude decay maps ([Fig. A3c, f](#)) generally
15 agrees with the empirical results ([Fig. 5c, f](#)), although now with a smaller variation in
16 amplitude. Note that because we do not consider attenuation in our simulation, the
17 corrected amplitude decay is solely due to the amplification effect (eq. A2). To estimate
18 the maximum amplification direction and amplitude, we again examine the directionally-
19 dependent corrected amplitude decay measurements (e.g. [Fig. A4a](#)). The observed
20 maximum amplification directions and amplitudes for the whole region are summarized
21 in [Figure A4b](#). The inverted amplification map after three iterations is shown in [Figure](#)

1 **A5a**, which now can be directly compared with the theoretical prediction based on our
2 input reference phase velocity map (**Fig. A5b-c**).

3 Overall, the constructed amplification map agrees well with the theoretical amplification
4 map. A cluster of discrepant points is observed in **Figure A5c** with larger than predicted
5 amplifications (observed>1.03; predicted<1.03). These points are mostly located near the
6 northwestern corner of the maps. The wavefield is not well constrained near the edge of
7 the station coverage, which results in higher uncertainty in the observed amplification.
8 The fact that the majority of the observed amplification is within 1% of the theoretical
9 prediction demonstrates the accuracy and robustness of the method.

10 **Acknowledgement**

11 The authors wish to thank B. Schmandt and R. W. Clayton for helpful discussions. The
12 facilities of the IRIS Data Management System, and specifically the IRIS Data
13 Management Center, were used to access the waveform and metadata required in this
14 study. The IRIS DMS is funded through the National Science Foundation and specifically
15 the GEO Directorate through the Instrumentation and Facilities Program of the National
16 Science Foundation under Cooperative Agreement EAR-0552316. This research was
17 supported by the Director's Post-Doctoral Fellowship of the Seismological Laboratory at
18 the California Institute of Technology and by NSF grants EAR-0711526 and
19 EAR-0844097 at the University of Colorado at Boulder.

20 **Reference list**

21 Dalton, C.A. & Ekström, G., 2006a, Constraints on global maps of phase velocity from
22 surface-wave amplitudes, *Geophys. J. Int.*, **167**, 820–826.

- 1 Dalton, C.A. & Ekström, G., 2006b, Global models of surface wave attenuation, *J.*
2 *Geophys. Res.*, **111**, B05317, doi:10.1029/2005JB003997.
- 3 Dalton, C. A., Ekström, G., & Dziewoński, A. M., 2008, The global attenuation structure
4 of the upper mantle, *J. Geophys. Res.*, **113**, B09303, doi:10.1029/2007JB005429.
- 5 Dziewonski, A.M. & Anderson, D.L., 1981. Preliminary reference Earth model, *Phys.*
6 *Earth planet. Inter.*, **25**, 297–356.
- 7 Ekstrom, G., Tromp, J. & Larson, E.W.F., 1997. Measurements and global models of
8 surface wave propagation, *J. geophys. Res.*, **102**, 8137–8157.
- 9 Gilbert, H., and Flesch, L.M., 2009. Using Earth- scope data to separate the influences of
10 inher- ited lithospheric structures and more recent tectonics in driving the
11 dynamics of the west- ern United States: Eos (Transactions, Ameri- can
12 Geophysical Union), v. 90, Fall meeting supplement., abs. U52A–05.
- 13 Herrmann, R. B., and C. J. Ammon (2004), Computer Programs in Seis- mology: Surface
14 Waves, Receiver Functions and Crustal Structure, St. Louis Univ., St. Louis, Mo.
- 15 Lawrence, J.F., & G.A. Prieto, 2011, Attenuation tomography of the western United
16 States from ambient seismic noise, *J. Geophys. Res.*, **116**, B06302,
17 doi:10.1029/2010JB007836.
- 18 Levshin, A.L., X. Yang, M.P. Barmin, and M.H. Ritzwoller, 2010, Mid-period Rayleigh
19 wave attenuation model for Asia, *Geochem. Geophys. Geosyst.*, **11**(8), Q08017,
20 doi:10.1029/2010GC003164.

- 1 Liang, C., & Langston, C. A., 2009. Wave gradiometry for USArray: Rayleigh waves, *J.*
2 *Geophys. Res.*, **114**, B02308, doi:10.1029/2008JB005918.
- 3 Lin, F., Moschetti, M.P. & Ritzwoller, M. H., 2008. Surface wave tomography of the
4 western United States from ambient seismic noise: Rayleigh and Love wave
5 phase velocity maps. *Geophys. J. Int.*, **173**(1), 281–298.
- 6 Lin, F., Ritzwoller, M.H. & Snieder, R., 2009. Eikonal tomography: surface wave
7 tomography by phase front tracking across a regional broad-band seismic array.
8 *Geophys. J. Int.*, **177**(3), 1091–1110.
- 9 Lin, F. and M.H. Ritzwoller, 2011a, Helmholtz surface wave tomography for isotropic
10 and azimuthally anisotropic structure, *Geophys. J. Int.*, **186**, 1104–1120.
- 11 Lin, F. and M.H. Ritzwoller, 2011b, Apparent anisotropy in inhomogeneous isotropic
12 media, *Geophys. J. Int.*, **186**, 1205–1219.
- 13 Lin, F., M.H. Ritzwoller, Y. Yang, M.P. Moschetti, and M.J. Fouch, 2011a. Complex and
14 variable crustal and uppermost mantle seismic anisotropy in the western
15 United States. *Nature Geoscience*, **4**, 55–61.
- 16 Lin, F., M.H. Ritzwoller, & W. Shen, 2011b, On the reliability of attenuation
17 measurements from ambient noise cross-correlations, *Geophys. Res. Lett.*, **38**,
18 L11303, doi:10.1029/2011GL047366.
- 19 Lowry, A. R., N. M. Ribe, and R. B. Smith 2000, Dynamic elevation of the Cordillera,
20 western United States, *J. Geophys. Res.*, **105**(B10), 23,371–23,390,
21 doi:10.1029/2000JB900182.

- 1 Jackson, I., Fitz Gerald, J., Faul, U. & Tan, B.H., 2002. Grain-size-sensitive seismic wave
2 attenuation in polycrystalline olivine, *J. Geophys. Res.*, **107**, 2360,
3 doi:10.1029/2001JB001225.
- 4 Maceira, M. and C. J. Ammon, 2009, Joint inversion of surface wave velocity and gravity
5 observations and its application to central Asian basins shear velocity structure, *J*
6 *Geophys Res*, **114**, B02314, doi:10.1029/2007JB005157.
- 7 Moschetti, M.P., Ritzwoller, M.H., Lin, F.C., & Yang, Y., 2010a. Seismic evidence for
8 widespread crustal deformation caused by extension in the western USA. *Nature*
9 **464** (N7290), 885–889.
- 10 Moschetti, M.P., Ritzwoller, M.H., Lin, F.C., & Yang, Y., 2010b. Crustal shear velocity
11 structure of the western US inferred from ambient noise and earthquake data. *J.*
12 *Geophys. Res.* **115**, B10306 doi:10.1029/ 2010JB007448.
- 13 Pollitz, F.F. , 2008. Observations and interpretation of fundamental mode Rayleigh
14 wavefields recorded by the Transportable Array (USArray), *Geophys. J. Int.*, **173**,
15 189-204.
- 16 Pollitz, F. F. & Snoke, J. A., 2010, Rayleigh-wave phase-velocity maps and three-
17 dimensional shear velocity structure of the western US from local non-plane
18 surface wave tomography. *Geophys. J. Int.*, **180**, 1153–1169.
- 19 Prieto, G. A., Lawrence, J.F., & Beroza, G.C., 2009. Anelastic Earth structure from the
20 coherency of the ambient seismic field, *J. Geophys. Res.*, **114**, B07303,
21 doi:10.1029/2008JB006067.

- 1 Shapiro, N.M., Campillo, M., Stehly, L. & Ritzwoller, M.H., 2005. High resolution
2 surface wave tomography from ambient seismic noise, *Science*, **307**(5715), 1615–
3 1618.
- 4 Smith, W.H.F. & Wessel, P., 1990. Gridding with continuous curvature splines in
5 tension, *Geophysics*, **55**, 293–305.
- 6 Tanimoto, T., 1990. Modelling curved surface wave paths: membrane surface wave
7 synthetics, *Geophys. J. Int.*, **102**, 89–100.
- 8 Tanimoto, T., 1991, Waveform Inversion for Three-Dimensional Density and *S* Wave
9 Structure, *J. Geophys. Res.*, **96**(B5), 8167–8189, doi:10.1029/91JB00196
- 10 Tanimoto, T. & Rivera, L., 2008. The ZH ratio method for long-period seismic data:
11 sensitivity kernels and observational techniques, *Geophys. J. Int.*, **172**, 187–198.
- 12 Trampert, J. & Woodhouse, J.H., 1996. High resolution global phase velocity
13 distributions, *Geophys. Res. Lett.*, **23**, 21–24.
- 14 Tromp, J. & Dahlen, F. A., 1992. Variational principles for surface wave propagation on
15 a laterally heterogeneous Earth-11. Frequency-domain JWKB theory, *Geophys. J.*
16 *Int.*, **109**, 599-619.
- 17 Tromp, J. & Dahlen, F.A., 1993. Variational principles for surface wave propagation on a
18 laterally heterogeneous Earth.3. Potential representation, *Geophys. J. Int.*, **112**,
19 195–209.
- 20 Tsai, V. C., 2011. Understanding the amplitudes of noise correlation measurements, *J.*
21 *Geophys. Res.*, **116**, B09311, doi:10.1029/2011JB008483.

- 1 Wielandt, E., 1993. Propagation and structural interpretation of non-plane waves,
2 *Geophys. J. Int.*, **113**, 45–53.
- 3 Yang, Y. & Forsyth, D., 2006a. Rayleigh wave phase velocities, small-scale convection,
4 and azimuthal anisotropy beneath southern California, *J. Geophys. Res.*, **111**,
5 B07306, doi:10.1029/2005JB004180.
- 6 Yang, Y. & Forsyth, D., 2006b. Regional tomographic inversion of the amplitude and
7 phase of Rayleigh waves with 2-D sensitivity kernels, *Geophys. J. Int.*, **166**,
8 1148–1160.
- 9 Yang, Y. & Forsyth, D., 2008, Attenuation in the upper mantle beneath Southern
10 California: Physical state of the lithosphere and asthenosphere, *J. Geophys. Res.*,
11 **113**, B03308, doi:10.1029/2007JB005118.
- 12 Yang, Y., Ritzwoller, M.H., Lin, F.C., Moschetti, M.P. & Shapiro, N.M., 2008. Structure
13 of the crust and uppermost mantle beneath the western United States revealed by
14 ambient noise and earthquake tomography, *J. geophys. Res.*, **113**, B12310,
15 doi:10.1029/2008JB005833.

16

17

18

19 **Figure Captions**

20 Figure 1. (a) Triangles identify the USArray stations used in this study. The red lines are
21 tectonic and other boundaries in the western US. CB: Columbia Basin; ST: Salton
22 Trough; YSRP: Yellowstone/Snake River Plain; CP: Colorado Plateau; WY: Wyoming;

1 SR: Southern Rockies; CO: Colorado; HLP: High Lava Plains. The star marks the
2 location shown in Fig. 6a and A4a. (b) The earthquakes used in this study. Circles mark
3 the location of the earthquakes, the star is the centre of our study region, and the lines
4 between circles and the star are great-circle paths. The yellow circle and path mark the
5 earthquake used in Fig. 2 and Fig. 3.

6 Figure 2. (a)–(b) The 60 s Rayleigh wave observed phase traveltimes and amplitude maps,
7 respectively, for the 2009 April 7 earthquake near the Kuril Islands ($M_s = 6.8$). The
8 stations where phase traveltimes and amplitude measurements are obtained are
9 shown as triangles. Contours are separated by intervals of 60 s in (a) and 100 nm s^{-1} in
10 (b). The arrows indicate the approximate direction of wave propagation.

11 Figure 3. (a) The apparent amplitude decay derived from Fig. 2a–b based on eq. (8). (b)
12 The focusing/defocusing correction term in eq. (8) derived from Fig. 2a. (c) The relation
13 between the apparent amplitude decay and the focusing/defocusing correction term based
14 on (a) and (b) where each point represents the result at a grid point on the maps. The
15 green dashed line is the best fitting straight line with a slope of -1. The value of the
16 intercept is also shown. (d) The corrected amplitude decay map derived from (a) and (b)
17 based on eq. (8). The arrows in (a), (b), and (d) indicate the approximate direction of
18 wave propagation.

19 Figure 4. (a)–(b) The 30 and 60 sec Rayleigh wave phase velocity maps constructed using
20 Helmholtz tomography (Lin & Ritzwoller 2011a).

21 Figure 5. (a)–(c) The average apparent amplitude decay, focusing/defocusing correction,
22 and corrected amplitude decay for all measurements obtained from waves propagating in

1 the southeast direction (120° to 150° azimuth angle). The arrows in (a)-(c) indicate the
2 approximate direction of wave propagation. (d)-(f) Same as (a)-(c) but for waves
3 propagating in the northwest direction (300° to 330° azimuth angle).

4 Figure 6. (a) The 60 s Rayleigh wave directionally dependent corrected amplitude decay
5 measurements at a point in western Wyoming (star in **Fig. 1a**). Each error bar is the mean
6 and the standard deviation of the mean of all measurements within each 20° bin. The solid
7 green line is the best fitting curve of a 360° -periodicity sine function. (b) The observed
8 60 s Rayleigh wave maximum amplification directions and amplification amplitudes. The
9 arrows present the maximum amplification directions with amplification amplitude larger
10 than $0.15 \cdot 10^{-3} \text{ s km}^{-2}$. The amplification amplitude is shown in the background.

11 Figure 7. (a) The 60 s Rayleigh wave amplification maps derived from the maximum
12 amplification directions and amplification amplitudes shown in **Figure 6b**. The triangles
13 show the station locations used in the inversion. (b)-(c) Same as (a) but after the 2nd and
14 3rd iterations.

15 Figure 8. (a) Same as **Figure 7c** but only the area with reliable constraints on Moho depth
16 (**Gilbert & Flesch 2009**) is shown. The amplification is normalized by the mean of the
17 amplification in the area and hence is slightly different than **Figure 7c**. (b) The predicted
18 60 sec Rayleigh wave amplification map based on the 3D velocity model with a vertically
19 and laterally homogeneous density structure (Model I). (c) Same as (b) but for the
20 vertically inhomogeneous density model (Model II) where a $\sim 20\%$ density jump is set
21 between the crust and mantle across the Moho. (d) The relation between the predicted
22 and observed amplification shown in (a) and (b) for density Model I where each point

1 represents the results at a grid point on the maps. The green dashed line is the reference
2 line for zero misfit. (e) Same as (d) but for the relation between (a) and (c), density
3 Model II.

4 Figure 9. Same as [Figure 8](#), but for the 30 sec Rayleigh wave.

5 Figure 10. The smoothed (average over a 4° radius circle) azimuthally weighted corrected
6 amplitude decay for the 30 sec and the 60 sec Rayleigh waves. The corresponding
7 approximated Q values are also shown in red beneath the color bar.

8 Figure 11. (a)-(c) The azimuthally weighted apparent amplitude decay,
9 focusing/defocusing correction, and corrected amplitude decay for all 60 sec Rayleigh
10 wave earthquake measurements.

11 Figure 12. (a)-(c) The depth sensitivity kernels of phase velocity, group velocity, the I_1
12 integral, and amplification for the 60 sec Rayleigh wave due to shear velocity (V_s solid
13 red line), compressional velocity (V_p green dashed line), and density (ρ blue dot-dashed
14 line) perturbations. (d)-(f) Same as (a)-(c) but for the 30 sec Rayleigh wave.

15 Figure A1. The reference phase velocity model used in the synthetic experiment. Within
16 the pink dashed line, the phase velocity map is equal to the map estimated by Helmholtz
17 tomography ([Lin & Ritzwoller 2011a](#)). The map is smoothly extrapolated to cover the
18 entire simulation area outside the dashed line. The eight stars mark the source locations
19 of the 2D simulations.

20 Figure A2. (a)-(b) Same as [Figure 2a-b](#) but the results derive from the synthetic
21 measurements for a source in the northwestern direction. (c)-(d) Same as (a)-(b) but for a

1 source in the southeastern direction. The amplitude contours are separated by intervals of
2 30 and 50 displacement unit in (b) and (d), respectively.

3 Figure A3. Same as **Figure 5**, but for the synthetic dataset.

4 Figure A4. Same as **Figure 6**, but for the synthetic dataset.

5 Figure A5. (a) Same as **Figure 7c**, but for the synthetic dataset. (b) The theoretical
6 amplification c'/c calculated based on the reference 60 sec Rayleigh wave phase velocity
7 map where c' is the reciprocal of the average slowness $1/c$ in the area. (c) The
8 relationship between the theoretical and observed amplification shown in (a) and (b)
9 where each point represents the result at a single grid point on the maps. The green
10 dashed line is the reference line for complete agreement.

11

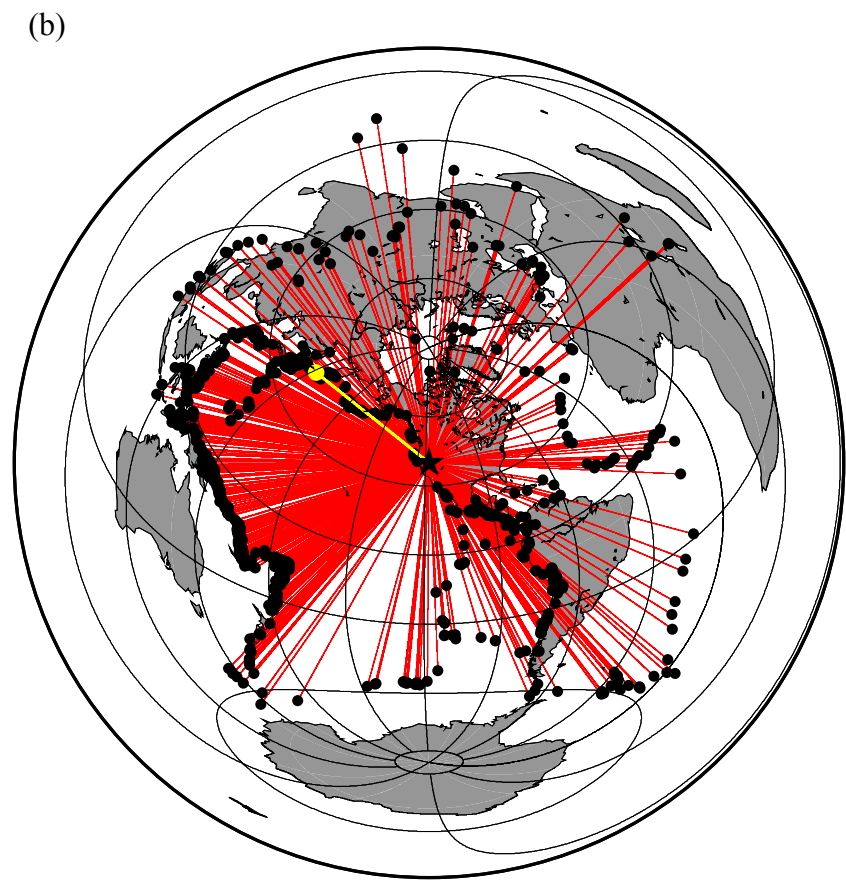
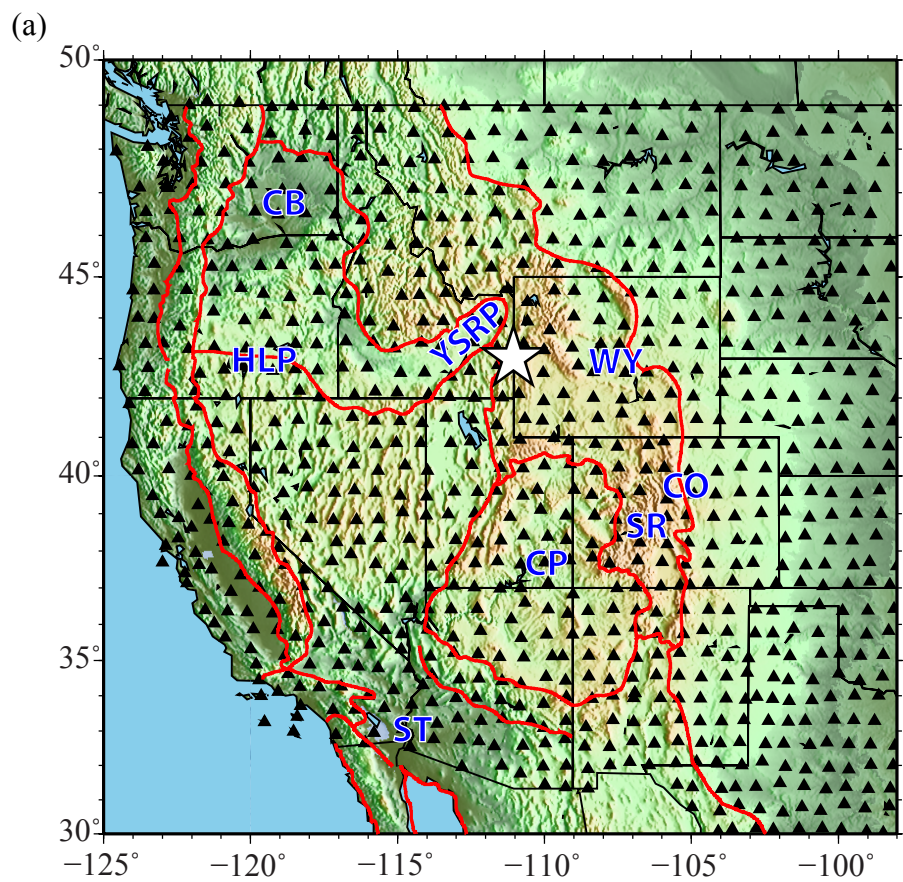


Figure 1

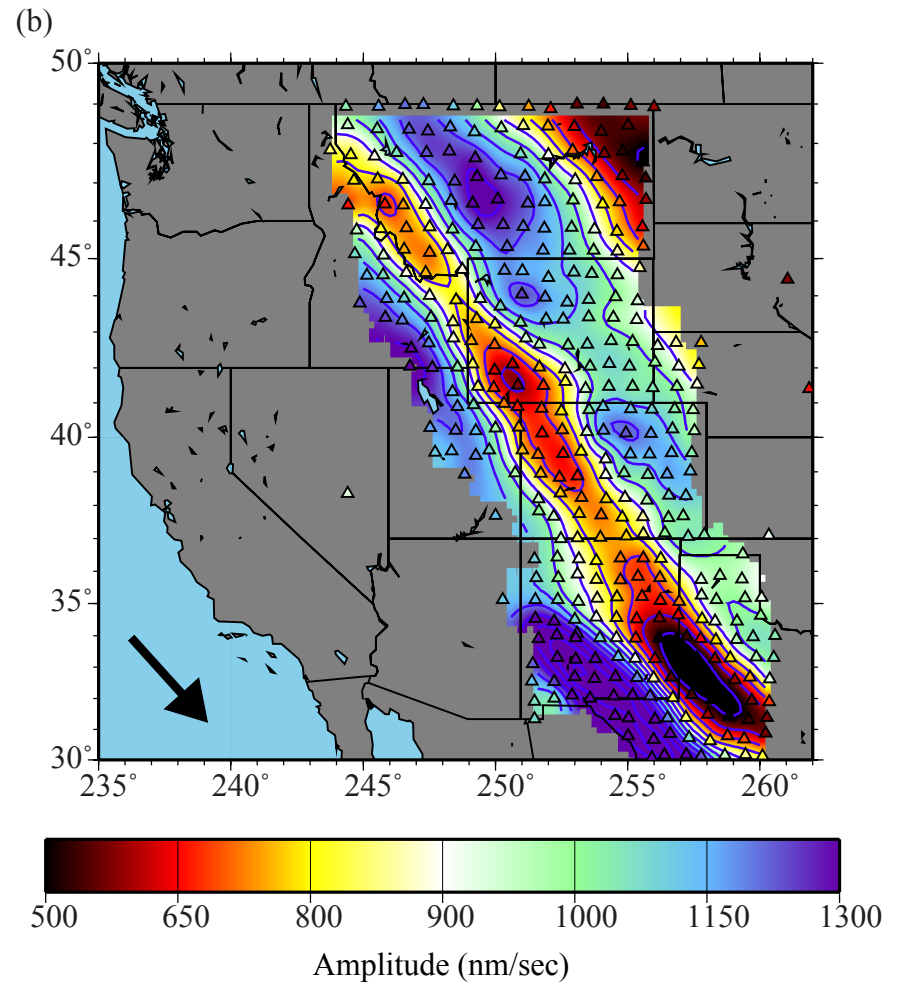
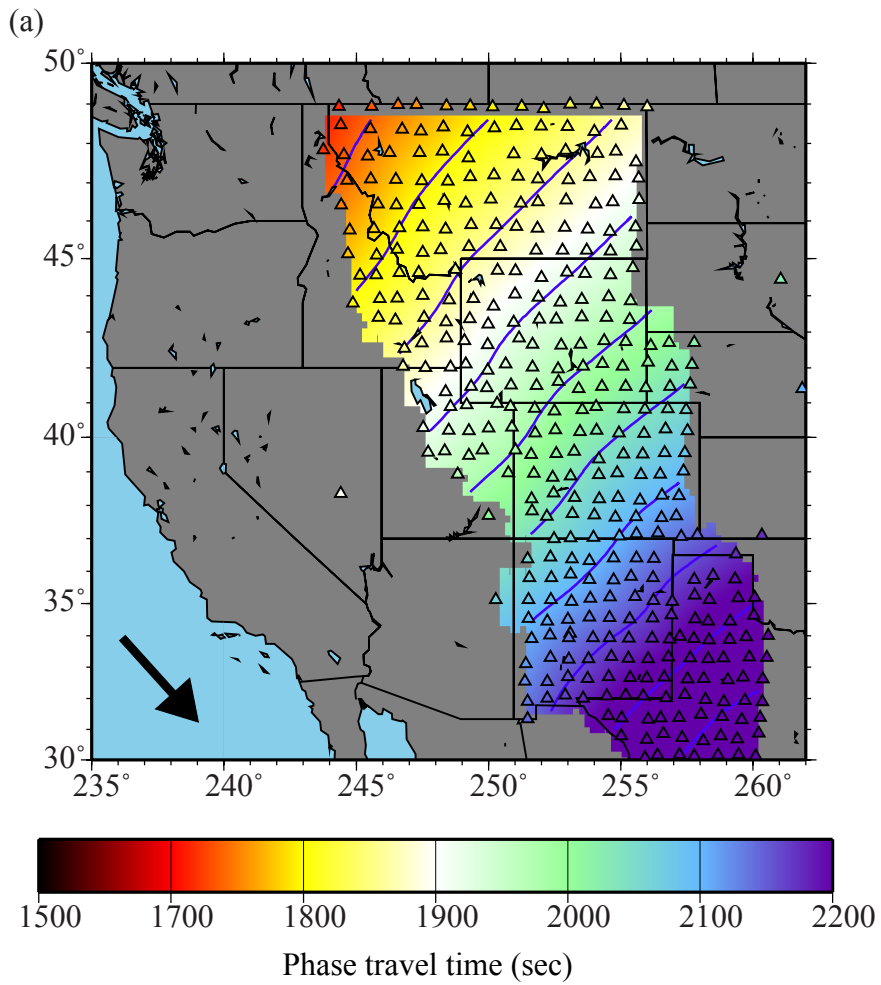


Figure 2.

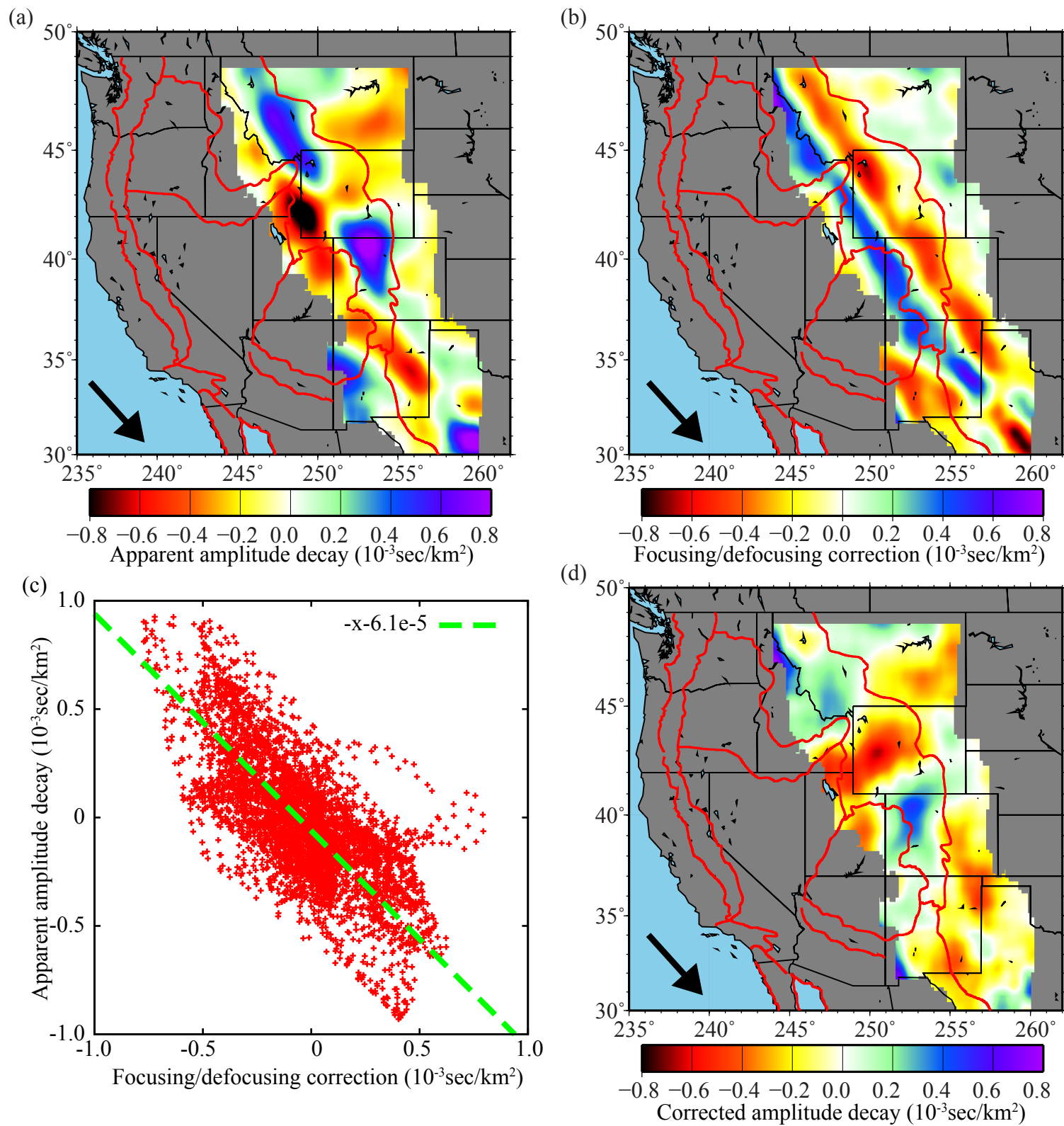


Figure 3.

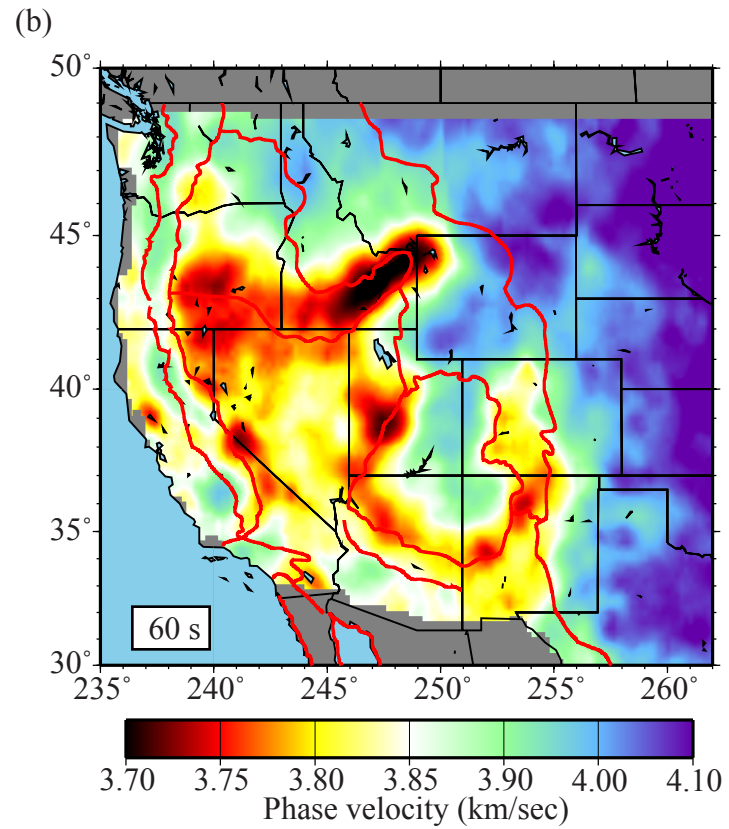
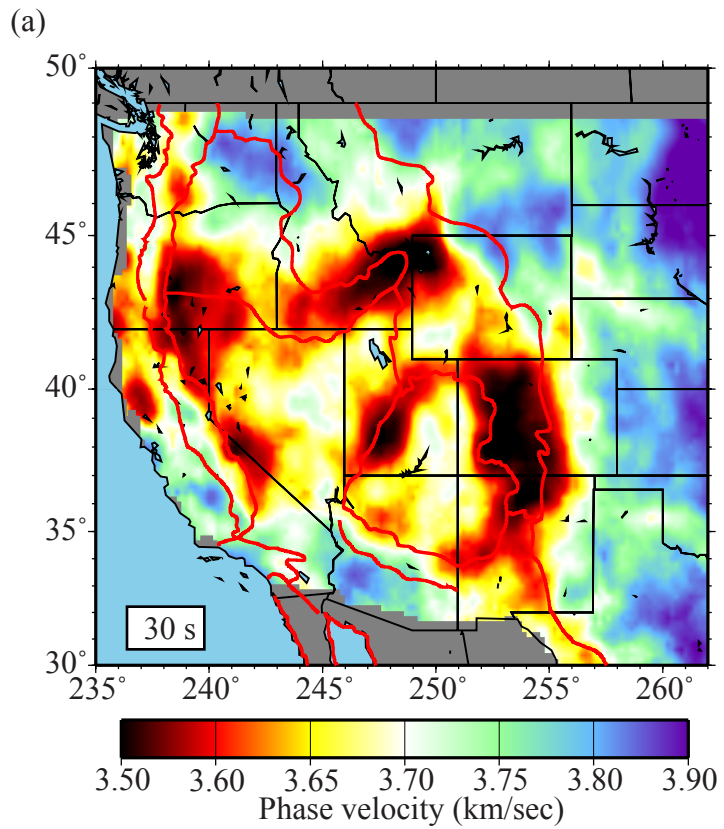


Figure 4

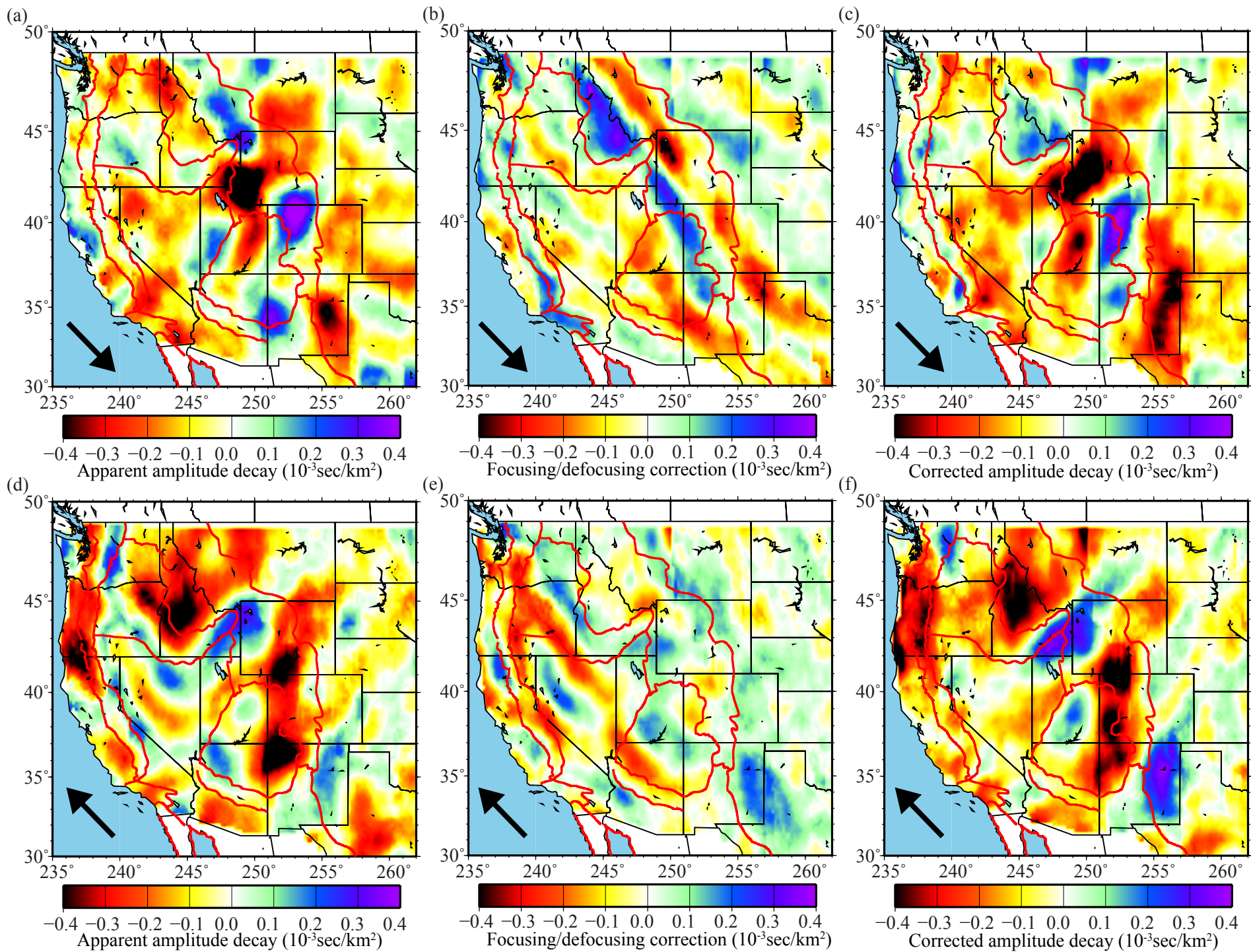


Figure 5.

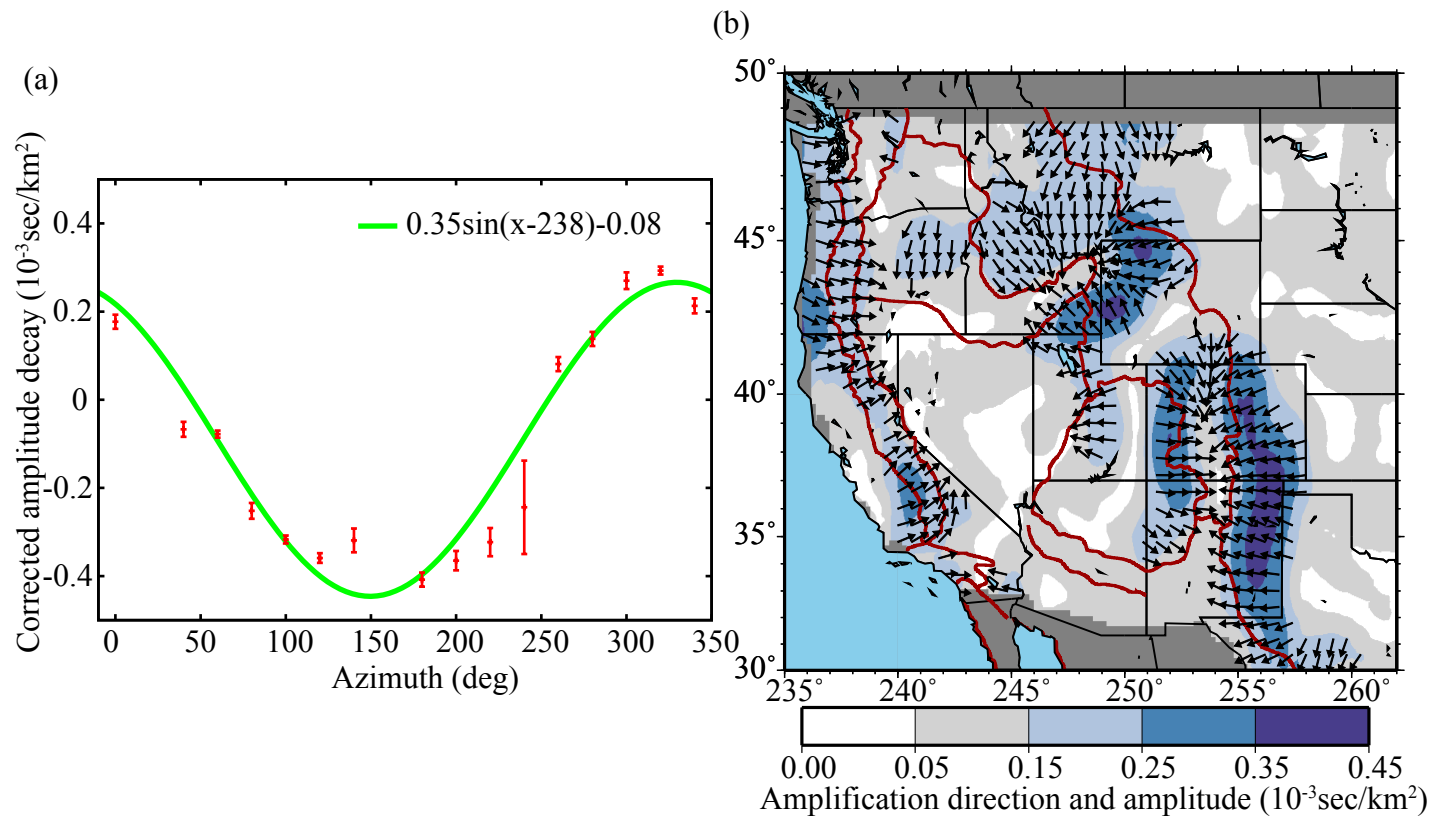


Figure 6.

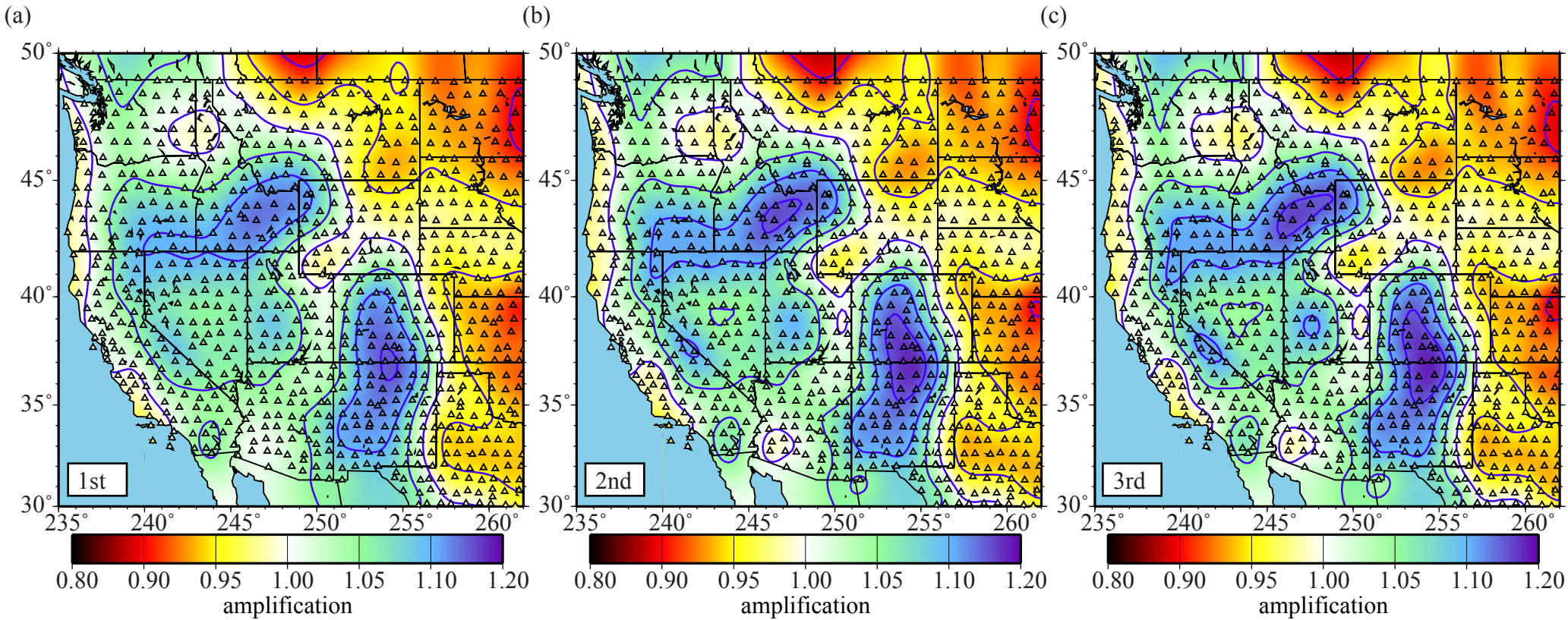


Figure 7.

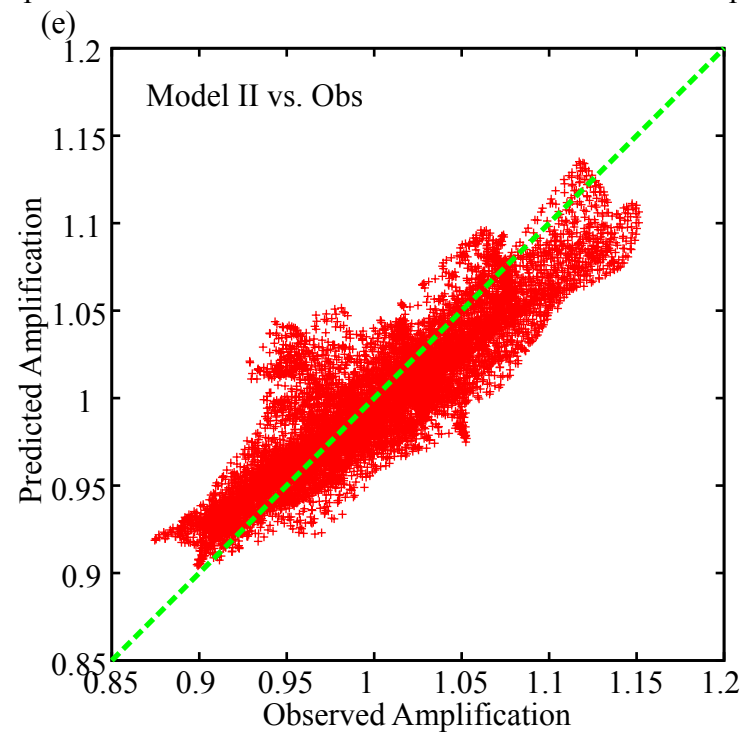
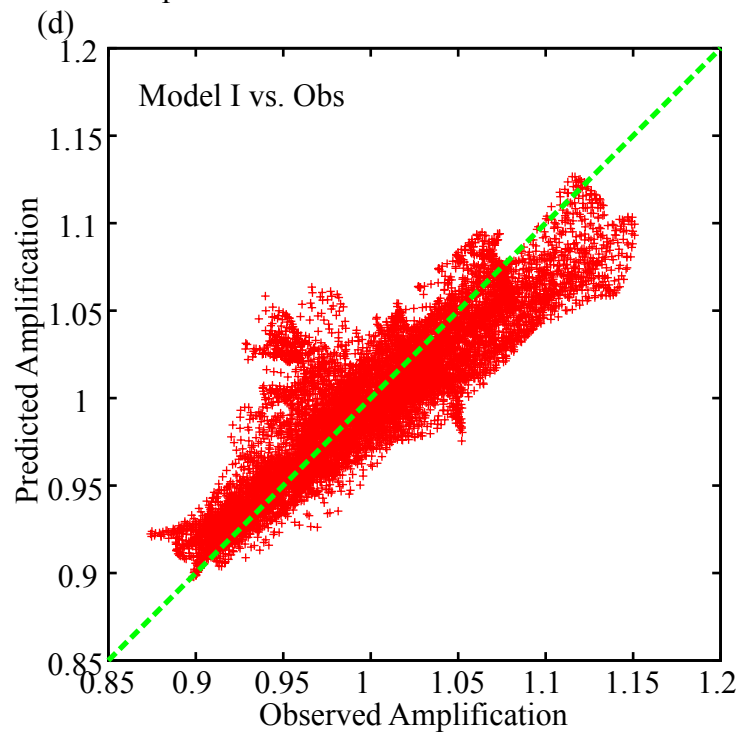
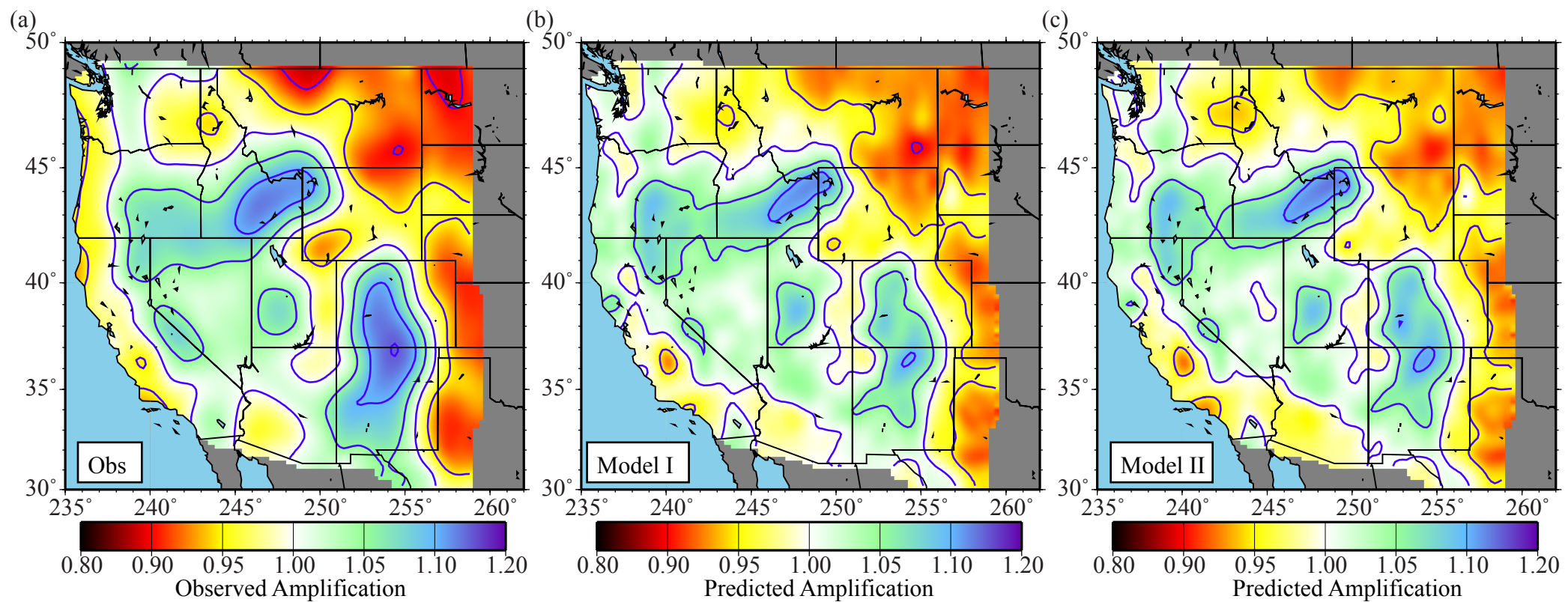


Fig. 8

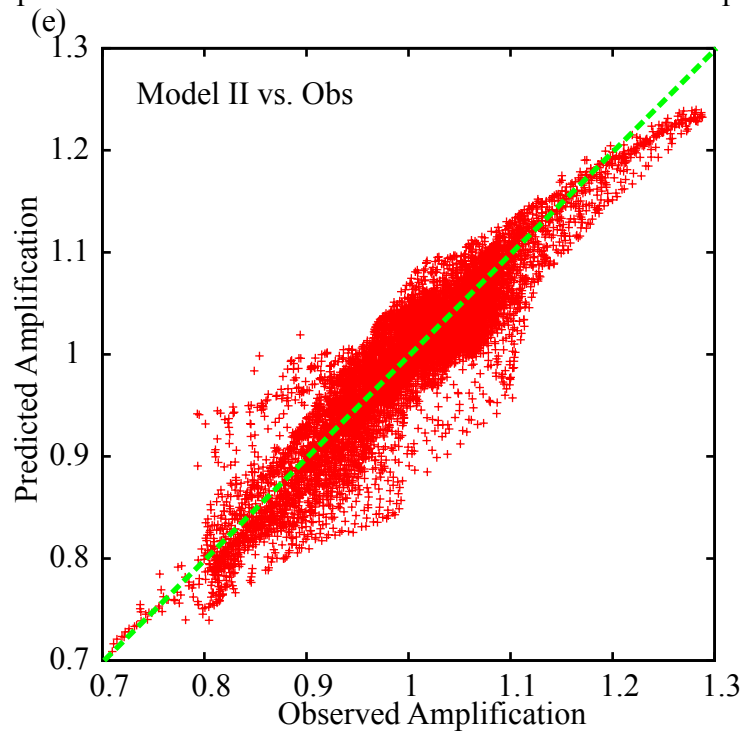
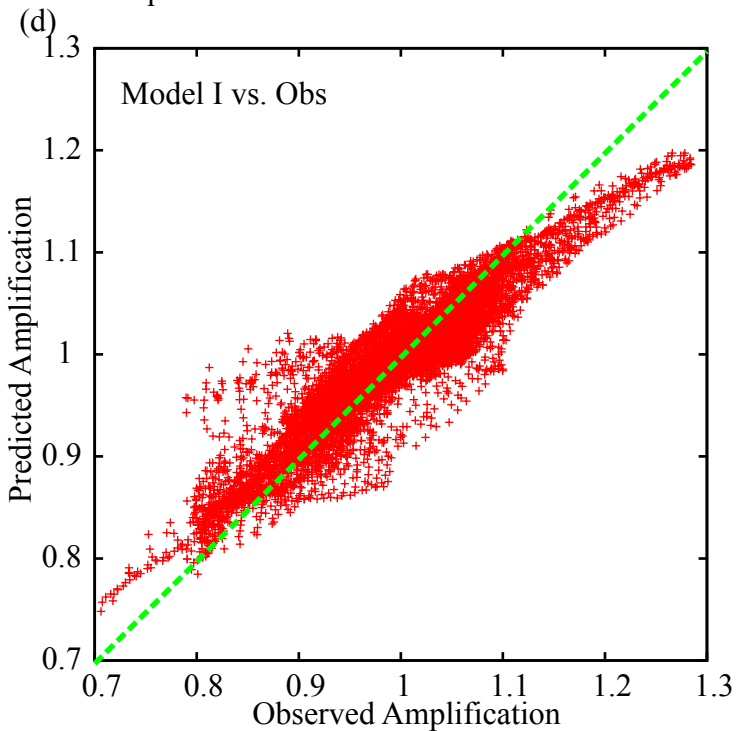
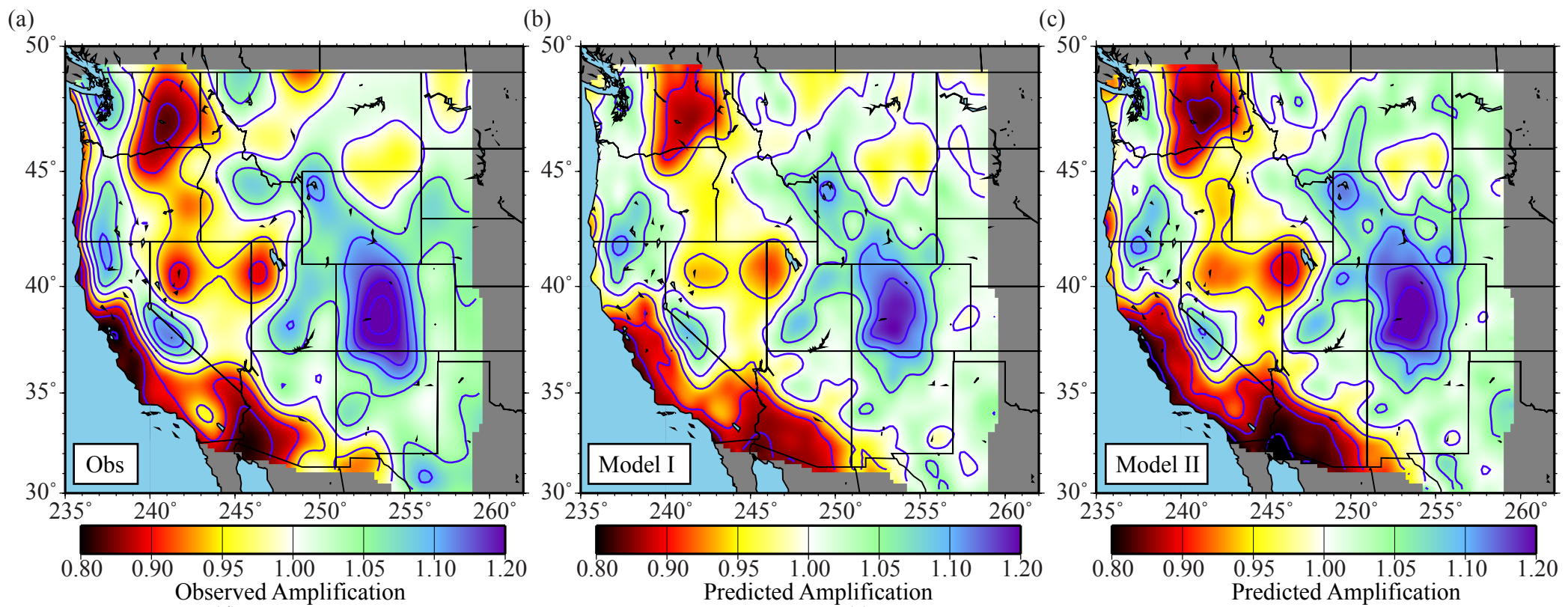


Fig. 9

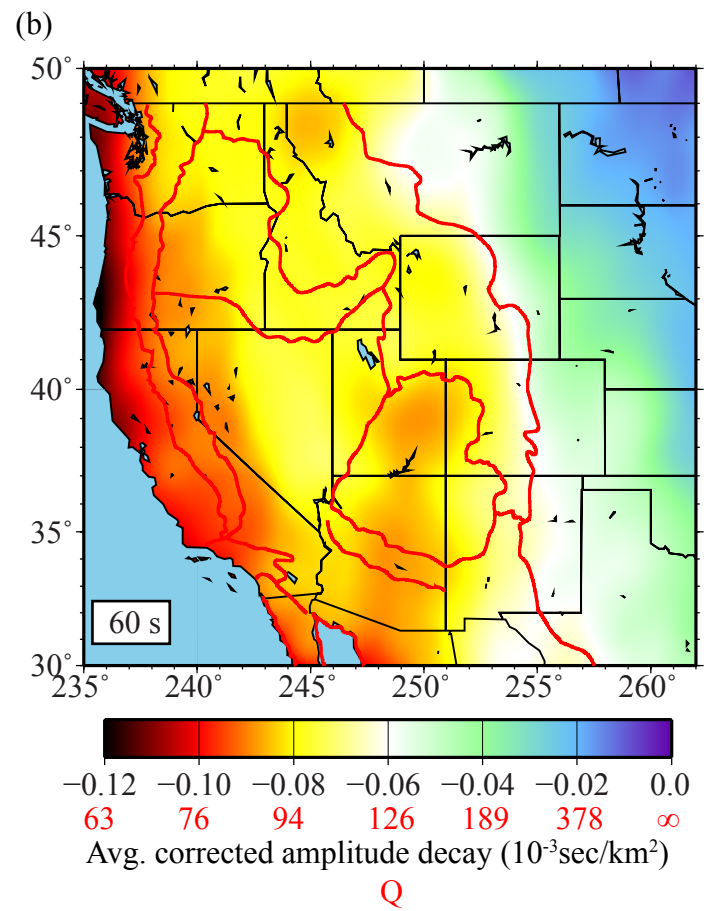
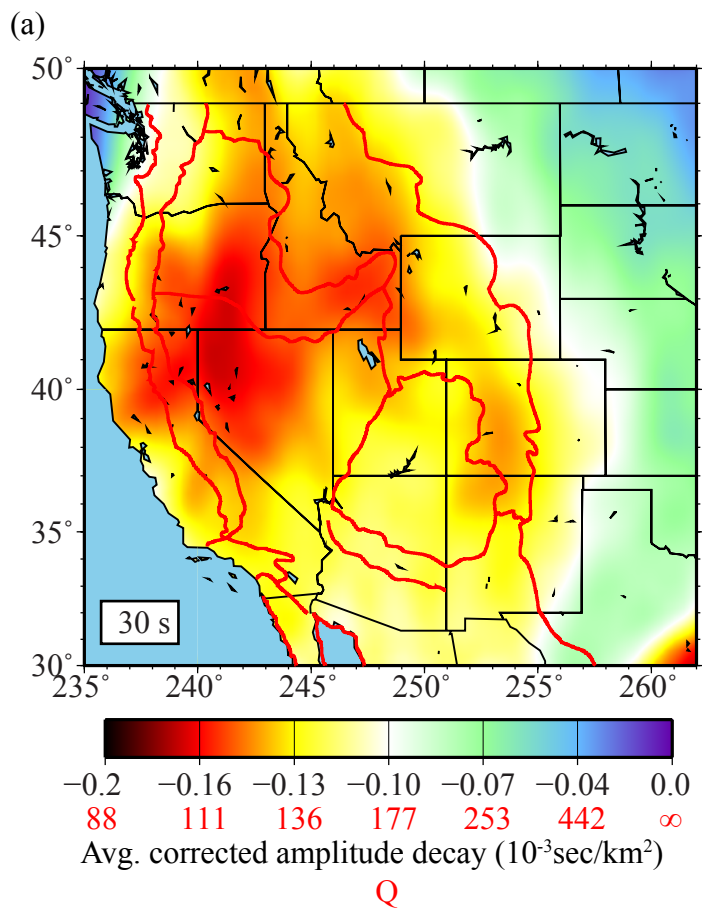


Figure 10.

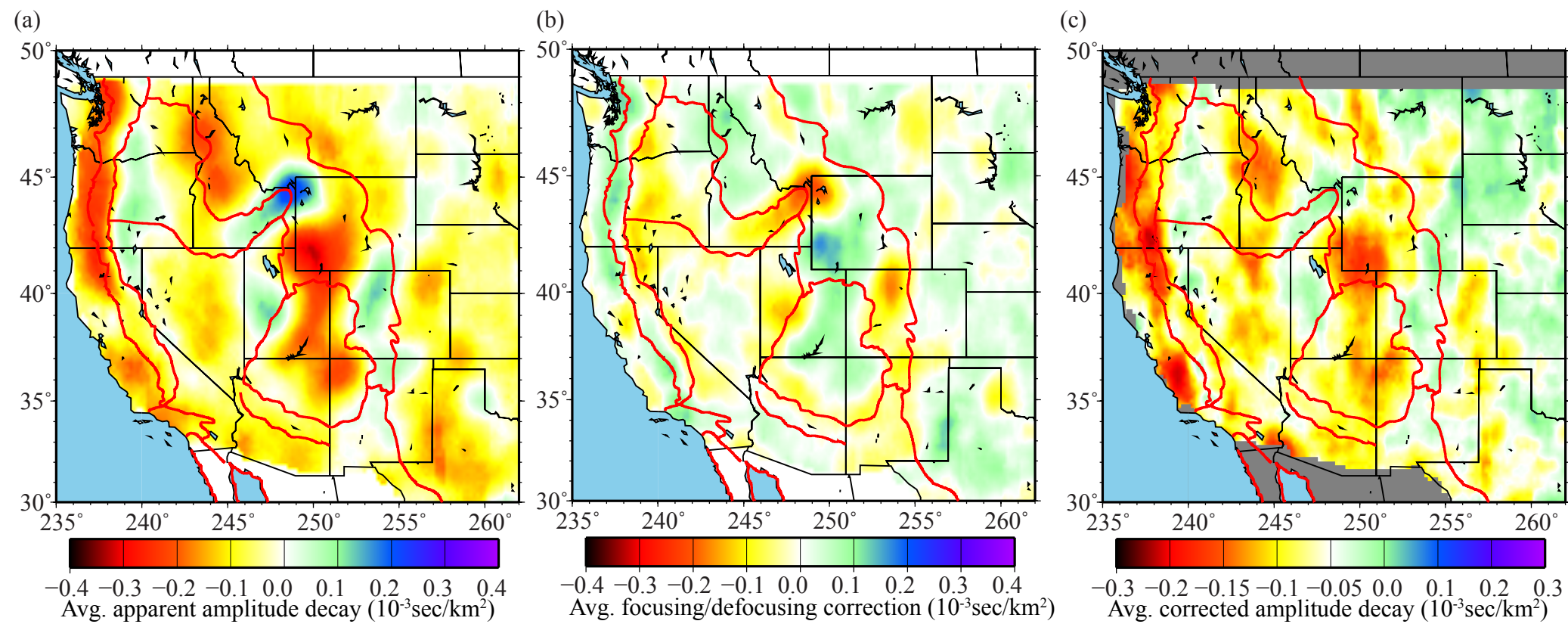


Figure 11.

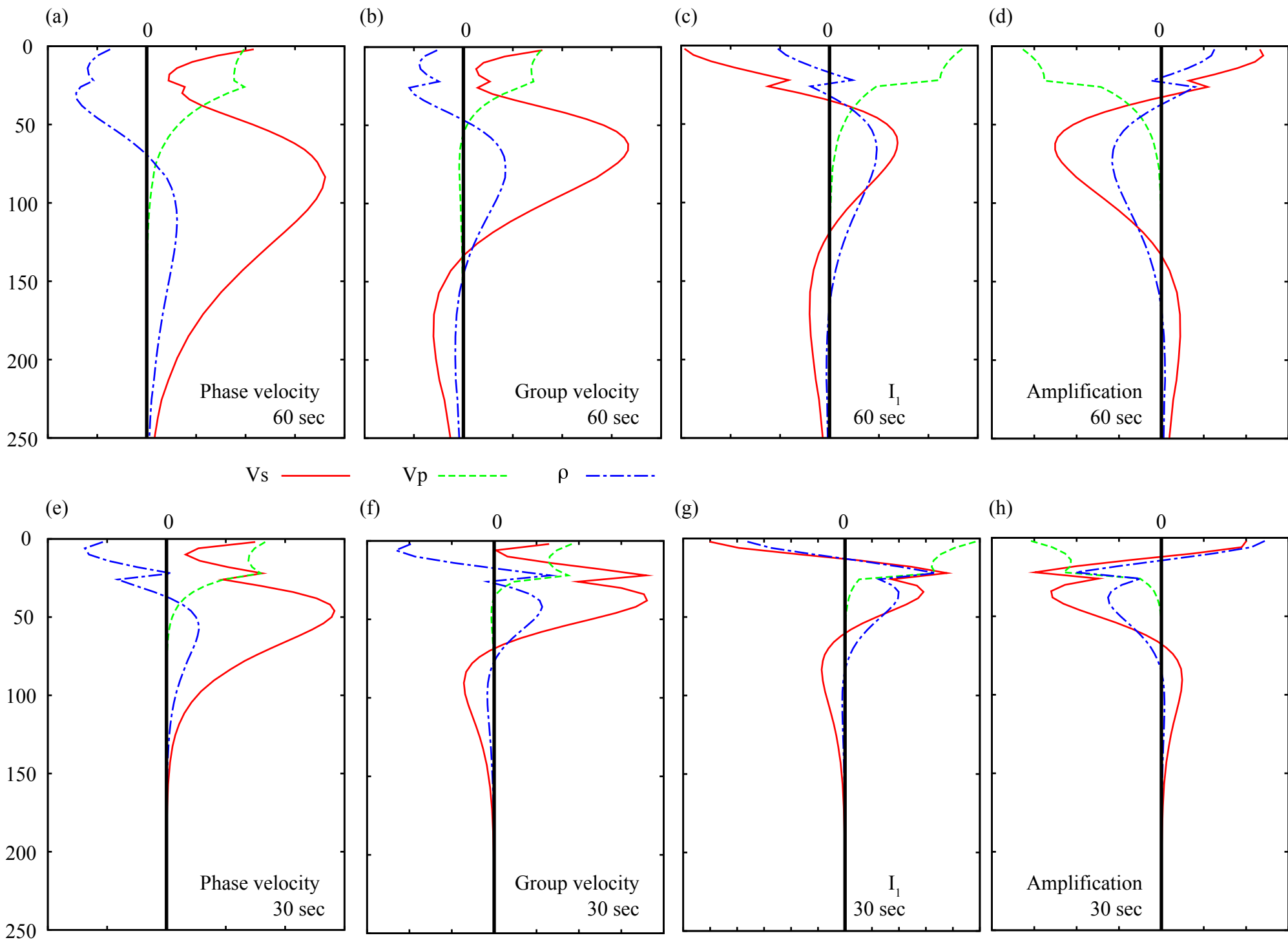


Figure 12

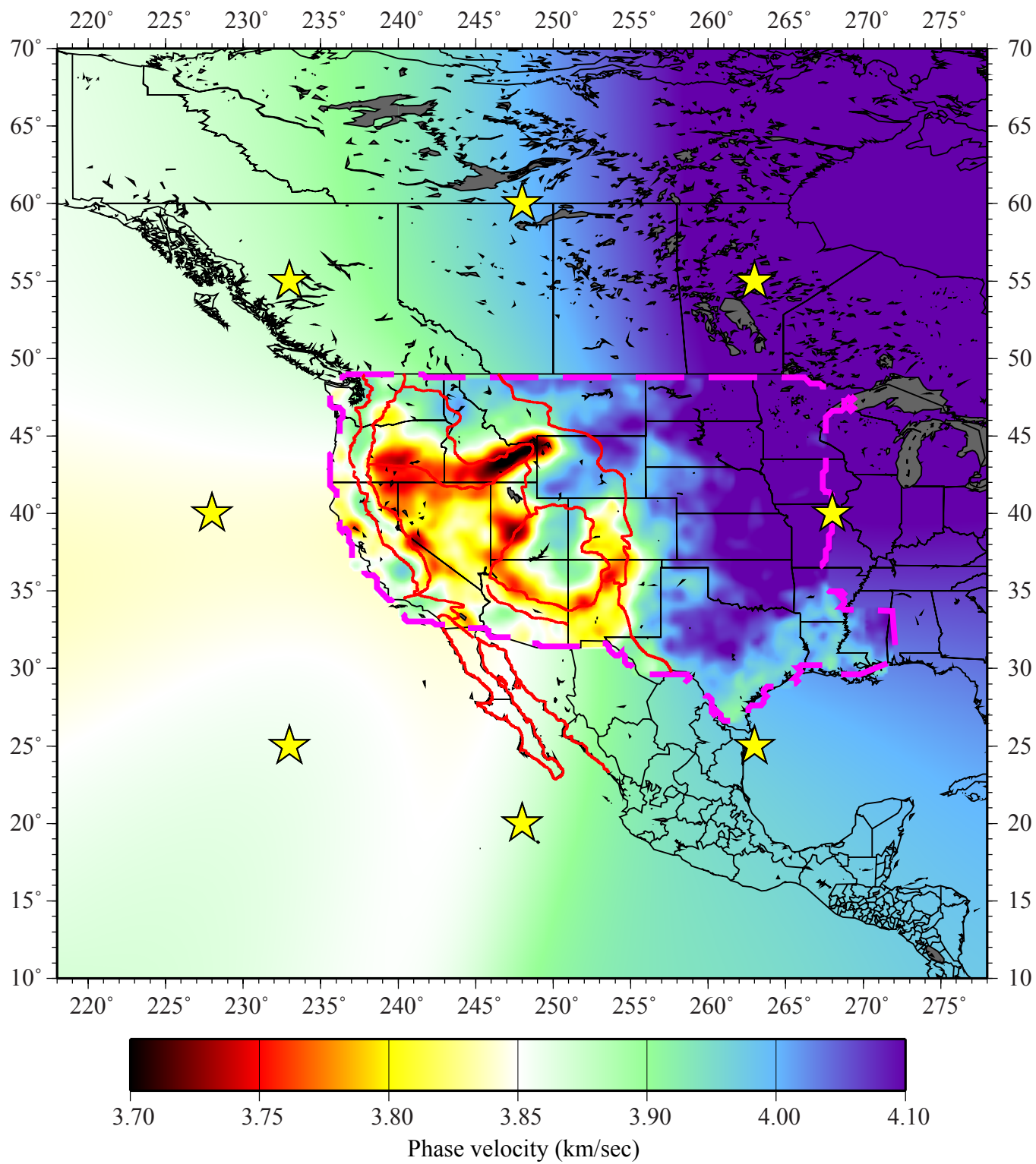


Figure A1

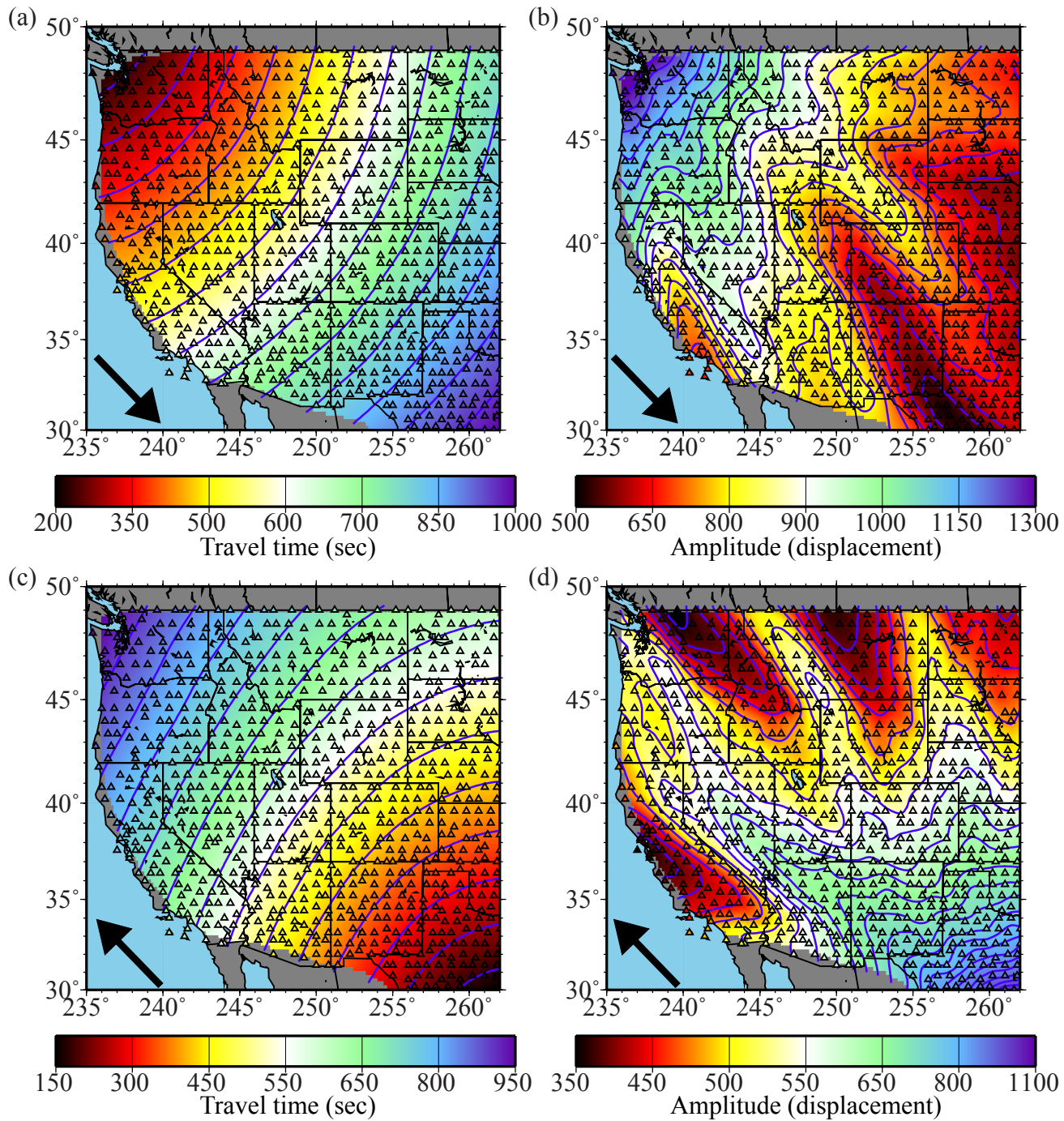


Figure A2

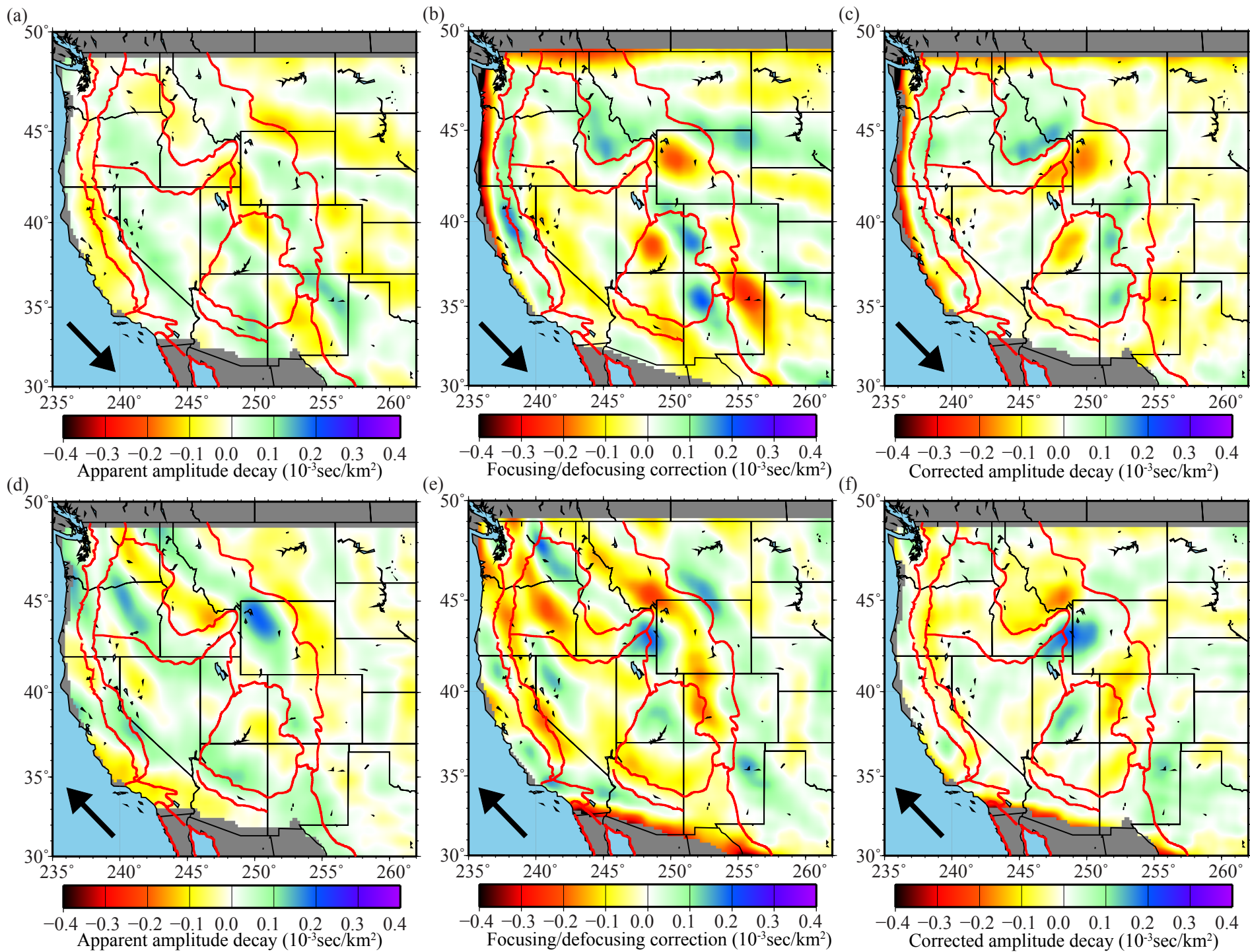


Figure A3

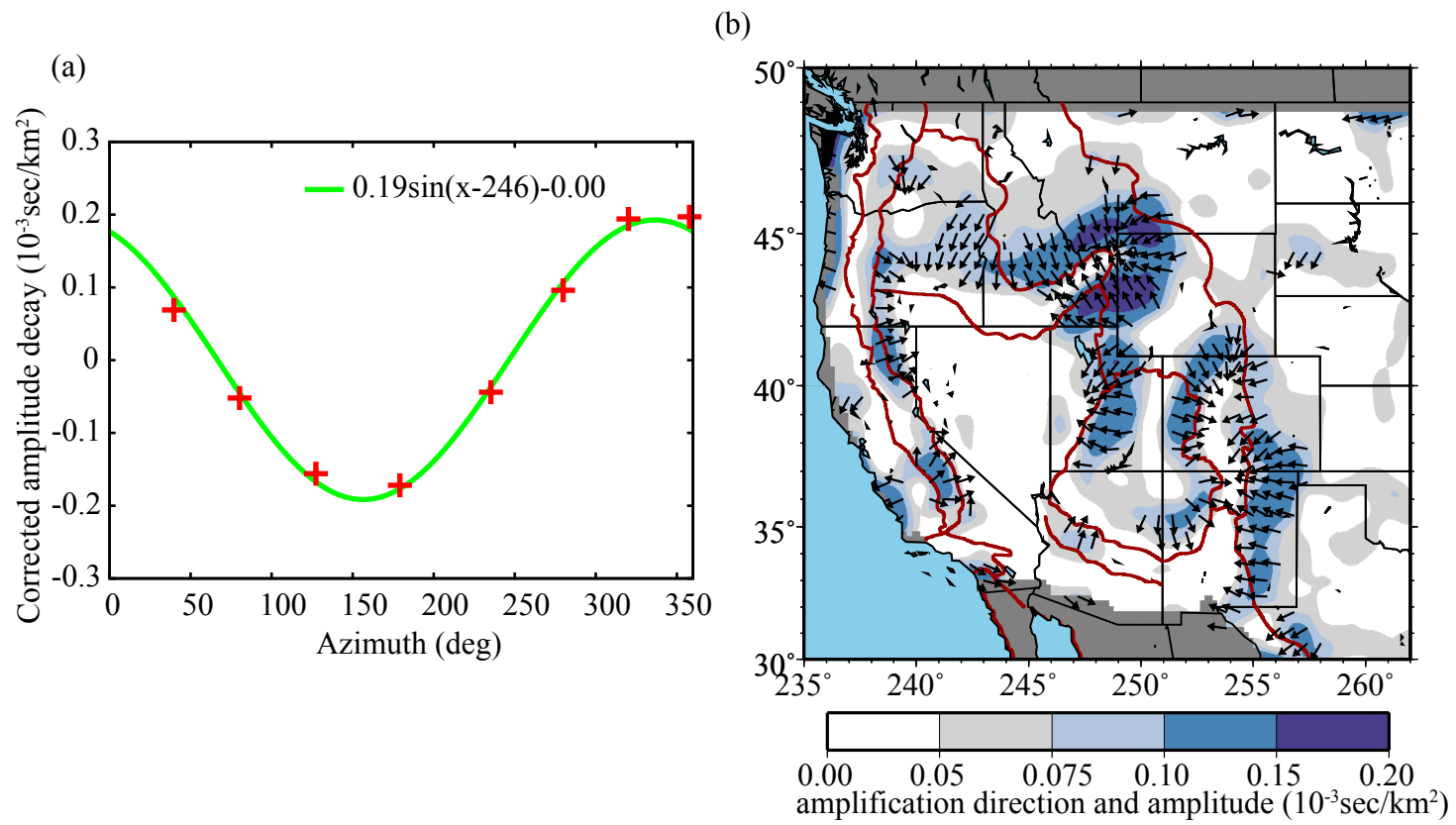


Figure A4

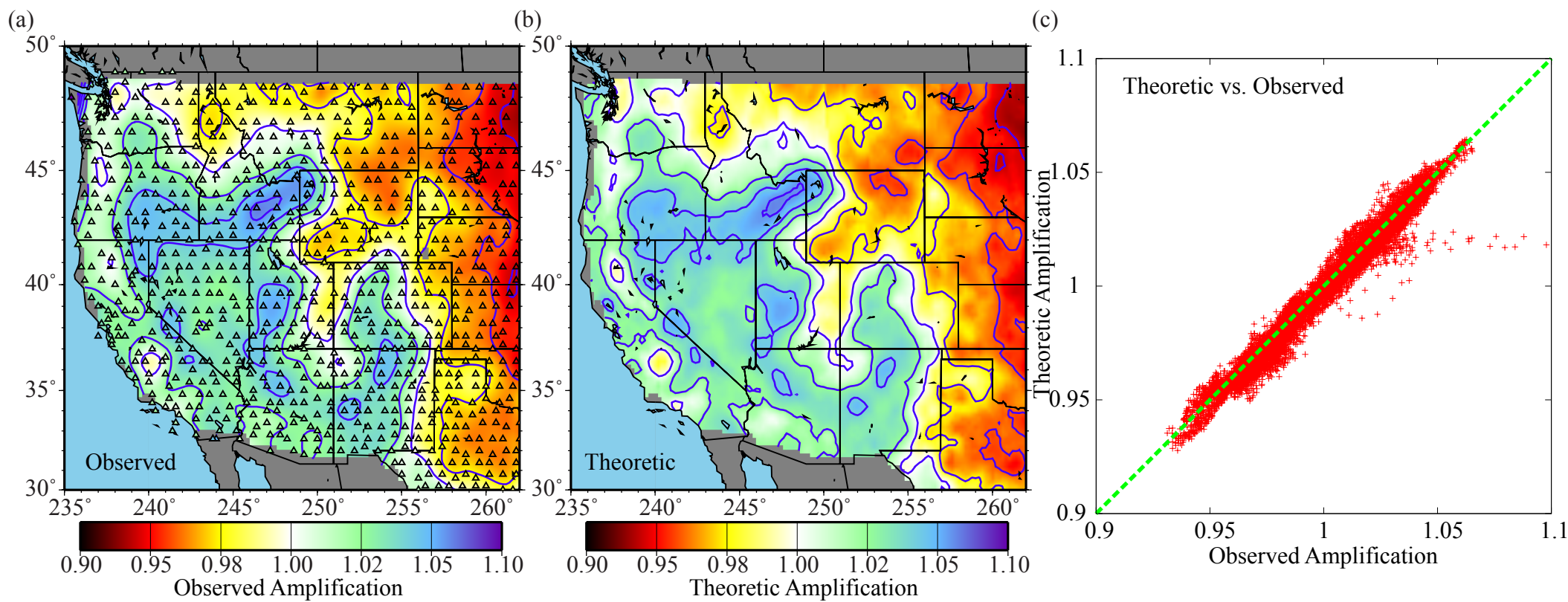


Fig. A5